

1

2

3

4

5

Simultaneous Measurement of Oscillation Parameters in Beam and Atmospheric Neutrino Data from Tokai-to-Kamioka and Super-Kamiokande Experiments

6

Daniel Robert Clement Barrow

7

8

Magdalen College,
Oxford University

9

Version 1.0

10

A Dissertation Submitted to Oxford University
11 for the Degree of Doctor of Philosophy

13 **Simultaneous Measurement of**
14 **Oscillation Parameters in Beam and**
15 **Atmospheric Neutrino Data from**
16 **Tokai-to-Kamioka and**
17 **Super-Kamiokande Experiments**

18 *Abstract*

19 Lorem ipsum dolor sit amet, consectetur adipiscing elit, sed do eiusmod tempor incididunt ut labore et dolore magna aliqua. Nulla aliquet porttitor lacus luctus accumsan tortor posuere. Pulvinar neque laoreet suspendisse interdum. Sem viverra aliquet eget sit. Nunc sed velit dignissim sodales ut eu sem integer vitae. At erat pellentesque adipiscing commodo elit at imperdiet dui accumsan. Fames ac turpis egestas integer eget aliquet nibh. Scelerisque eu ultrices vitae auctor eu augue. Purus non enim praesent elementum facilisis leo vel. Sollicitudin nibh sit amet commodo. Vitae auctor eu augue ut. Vel quam elementum pulvinar etiam. A condimentum vitae sapien pellentesque habitant morbi tristique senectus. Viverra accumsan in nisl nisi scelerisque eu ultrices. Sed viverra ipsum nunc aliquet bibendum enim. Sit amet purus gravida quis. In vitae turpis massa sed elementum tempus egestas sed sed. Vivamus arcu felis bibendum ut tristique et egestas. Senectus et netus et malesuada fames ac turpis. Ac auctor augue mauris augue.

35

Declaration

36

This dissertation is the result of my own work, except where explicit reference is made to the work of others, and has not been submitted for another qualification to this or any other university. This dissertation does not exceed the word limit for the respective Degree Committee.

37

38

39

40

41

Daniel Robert Clement Barrow

42

43

44

45

46

©The copyright of this thesis rests with the author and is made available under a Creative Commons Attribution Non-Commercial No Derivatives licence. Researchers are free to copy, distribute or transmit the thesis on the condition that they attribute it, that they do not use it for commercial purposes and that they do not alter, transform or build upon it. For any reuse or redistribution, researchers must make clear to others the licence terms of this work.

47

Acknowledgements

48 at pretium nibh ipsum. Eget nunc scelerisque viverra mauris in aliquam. Arcu vitae
49 elementum curabitur vitae nunc sed velit dignissim. Sed arcu non odio euismod lacinia
50 at quis risus sed. Vitae tempus quam pellentesque nec nam aliquam sem et tortor.
51 Viverra aliquet eget sit amet tellus cras adipiscing. Purus sit amet luctus venenatis
52 lectus magna. In aliquam sem fringilla ut morbi tincidunt augue. Fermentum dui
53 faucibus in ornare. Aliquam malesuada bibendum arcu vitae elementum curabitur
54 vitae nunc sed.

55 Ultricies leo integer malesuada nunc vel risus commodo. Tellus cras adipiscing
56 enim eu turpis egestas pretium. Dictumst quisque sagittis purus sit amet volutpat
57 consequat mauris nunc. Vitae congue mauris rhoncus aenean vel elit scelerisque
58 mauris pellentesque. Vel facilisis volutpat est velit egestas dui id ornare. Suscipit
59 adipiscing bibendum est ultricies. At in tellus integer feugiat scelerisque varius
60 morbi enim. Cras semper auctor neque vitae tempus. Commodo sed egestas egestas
61 fringilla phasellus faucibus. Cras pulvinar mattis nunc sed blandit. Pretium viverra
62 suspendisse potenti nullam ac tortor vitae. Purus sit amet volutpat consequat. Orci
63 sagittis eu volutpat odio facilisis mauris. Sit amet massa vitae tortor condimentum
64 lacinia quis. Commodo sed egestas egestas fringilla phasellus. Sed libero enim sed
65 faucibus turpis. Vitae tempus quam pellentesque nec.

66 Blandit massa enim nec dui. Viverra tellus in hac habitasse platea dictumst vestibulum.
67 Bibendum enim facilisis gravida neque convallis. Sagittis nisl rhoncus mattis
68 rhoncus urna neque. Nisl rhoncus mattis rhoncus urna neque. Ac tortor vitae purus
69 faucibus ornare. Aenean sed adipiscing diam donec adipiscing tristique risus. Sapien
70 nec sagittis aliquam malesuada bibendum. Et leo duis ut diam quam nulla. Tellus
71 rutrum tellus pellentesque eu tincidunt tortor aliquam nulla facilisi. Fermentum leo
72 vel orci porta non pulvinar neque. Eget sit amet tellus cras adipiscing enim eu. Sed
73 viverra tellus in hac habitasse platea dictumst vestibulum.

74 Sit amet consectetur adipiscing elit. At varius vel pharetra vel turpis nunc eget
75 lorem. Elit scelerisque mauris pellentesque pulvinar pellentesque habitant morbi
76 tristique senectus. Odio euismod lacinia at quis risus sed vulputate odio. Vitae suscipit
77 tellus mauris a diam maecenas sed enim ut. Dignissim convallis aenean et tortor at
78 risus viverra. Diam sollicitudin tempor id eu. Erat velit scelerisque in dictum. Blandit
79 cursus risus at ultrices. Ac tortor vitae purus faucibus ornare suspendisse sed.

⁸⁰ Contents

⁸¹ 1	Neutrino Oscillation Physics	¹
⁸² 1.1	Discovery of Neutrinos	¹
⁸³ 1.2	Theory of Neutrino Oscillation	³
⁸⁴ 1.2.1	Three Flavour Oscillations	³
⁸⁵ 1.2.2	The MSW Effect	⁷
⁸⁶ 1.3	Neutrino Oscillation Measurements	⁹
⁸⁷ 1.3.1	Solar Neutrinos	⁹
⁸⁸ 1.3.2	Atmospheric Neutrinos	¹²
⁸⁹ 1.3.3	Accelerator Neutrinos	¹⁵
⁹⁰ 1.3.4	Reactor Neutrinos	¹⁸
⁹¹ 2	T2K and SK Experiment Overview	²¹
⁹² 2.1	The Super-Kamiokande Experiment	²¹
⁹³ 2.1.1	The SK Detector	²²
⁹⁴ 2.1.2	Calibration	²⁶
⁹⁵ 2.1.3	Data Acquisition and Triggering	²⁹
⁹⁶ 2.1.4	Cherenkov Radiation	³¹
⁹⁷ 2.2	The Tokai to Kamioka Experiment	³³
⁹⁸ 2.2.1	The Neutrino Beam	³⁵
⁹⁹ 2.2.2	The Near Detector at 280m	³⁸
¹⁰⁰ 2.2.2.1	Fine Grained Detectors	⁴¹
¹⁰¹ 2.2.2.2	Time Projection Chambers	⁴²
¹⁰² 2.2.2.3	π^0 Detector	⁴⁴
¹⁰³ 2.2.2.4	Electromagnetic Calorimeter	⁴⁴
¹⁰⁴ 2.2.2.5	Side Muon Range Detector	⁴⁶
¹⁰⁵ 2.2.3	The Interactive Neutrino GRID	⁴⁶
¹⁰⁶ 3	Bayesian Statistics and Markov Chain Monte Carlo Techniques	⁴⁸
¹⁰⁷ 3.1	Bayesian Statistics	⁴⁹
¹⁰⁸ 3.2	Monte Carlo Simulation	⁵⁰
¹⁰⁹ 3.2.1	Markov Chain Monte Carlo	⁵²
¹¹⁰ 3.2.2	Metropolis-Hastings Algorithm	⁵⁵
¹¹¹ 3.2.3	MCMC Optimisation	⁵⁶

112	3.3 Understanding the MCMC Results	60
113	3.3.1 Marginalisation	60
114	3.3.2 Parameter Estimation and Credible Intervals	61
115	3.3.3 Application of Bayes' Theorem	63
116	3.3.4 Comparison of MCMC Output to Expectation	64
117	4 Oscillation Probability Calculation	66
118	4.1 Overview	66
119	Bibliography	71
120	List of Figures	78
121	List of Tables	82

¹²³ **Chapter 1**

¹²⁴ **Neutrino Oscillation Physics**

¹²⁵ When first proposed, neutrinos were expected to be massless fermions that only in-
¹²⁶ teract through weak and gravitational forces. This meant they were very difficult to
¹²⁷ detect as they can pass through significant amounts of matter without interacting. De-
¹²⁸ spite this, experimental neutrino physics has developed with many different detection
¹²⁹ techniques and neutrino sources being used today. In direct tension with the standard
¹³⁰ model physics, neutrinos have been determined to oscillate between different lepton
¹³¹ flavours requiring them to have mass.

¹³² section 1.1 describes the observation techniques and discovery of neutrinos. The
¹³³ theory underpinning neutrino oscillation is described in section 1.2. This section
¹³⁴ includes the approximations which can be made to simplify the understanding of
¹³⁵ neutrino oscillation in a two-flavour approximation as well as how the medium
¹³⁶ in which neutrinos propagate can manipulate the oscillation probability. The past,
¹³⁷ current, and future neutrino experiments are detailed in section 1.3 including the
¹³⁸ reactor, atmospheric, and long-baseline accelerator neutrino sources that have been
¹³⁹ used to successfully constrain oscillation parameter determination.

¹⁴⁰ **1.1 Discovery of Neutrinos**

¹⁴¹ At the start of the 20th century, the electrons emitted from the β -decay of the nucleus
¹⁴² were found to have a continuous energy spectrum [1,2]. This observation seemingly
¹⁴³ broke the energy conservation invoked within that period's nuclear models. Postulated

¹⁴⁴ in 1930 by Pauli as the solution to this problem, the neutrino (originally termed
¹⁴⁵ “neutron”) was theorized to be an electrically neutral spin-1/2 fermion with a mass of
¹⁴⁶ the same order of magnitude as the electron [3]. This neutrino was to be emitted with
¹⁴⁷ the electron in β -decay to alleviate the apparent breaking of energy conservation. As a
¹⁴⁸ predecessor of the weak interaction model, Fermi’s theory of β -decay developed the
¹⁴⁹ understanding by coupling the four constituent particles; electron, proton, neutron,
¹⁵⁰ and neutrino, into a consistent model [4].

¹⁵¹ Whilst Pauli was not convinced of the ability to detect neutrinos. The first observa-
¹⁵² tions of the particle were made in the mid-1950s when neutrinos from a reactor were
¹⁵³ observed via the inverse β -decay (IBD) process, $\bar{\nu}_e + p \rightarrow n + e^+$ [5, 6]. The detector
¹⁵⁴ consisted of two parts; a neutrino interaction medium and a liquid scintillator. The
¹⁵⁵ interaction medium was built from two water tanks. These were loaded with cadmium
¹⁵⁶ chloride to allow increased efficiency of neutron capture. The positron emitted from
¹⁵⁷ IBD annihilates, $e^+ + e^- \rightarrow 2\gamma$, generating a prompt signal and the neutron is captured
¹⁵⁸ on the cadmium via $n + ^{108}Cd \rightarrow ^{109}Cd \rightarrow ^{109}Cd + \gamma$, producing a delayed signal.
¹⁵⁹ The experiment observed an increase in the neutrino event rate when the reactor was
¹⁶⁰ operating compared to when it was switched off, in much the same way as modern
¹⁶¹ reactor neutrino experiments operate.

¹⁶² After the discovery of the ν_e , the natural question of how many flavours of neutrino
¹⁶³ exist was asked. In 1962, a measurement of the ν_μ was conducted at the Brookhaven
¹⁶⁴ National Laboratory [7]. A proton beam was directed at a beryllium target, generating
¹⁶⁵ a π -dominated beam which then decayed via $\pi^\pm \rightarrow \mu^\pm + (\nu_\mu, \bar{\nu}_\mu)$, and the subsequent
¹⁶⁶ interactions of the ν_μ were observed. The final observation to be made was that of the
¹⁶⁷ ν_τ from the DONUT experiment [8]. Three neutrinos seem the obvious solution as it
¹⁶⁸ mirrors the known number of charged lepton (as they form weak isospin doublets) but
¹⁶⁹ there could be evidence of more. Several neutrino experiments have found anomalous

₁₇₀ results [9, 10] which could be attributed to sterile neutrinos however cosmological
₁₇₁ observations indicate the number of neutrino species $N_{eff} = 3.15 \pm 0.23$ [11].

₁₇₂ 1.2 Theory of Neutrino Oscillation

₁₇₃ As direct evidence of beyond Standard Model physics, a neutrino generated with
₁₇₄ lepton flavour α can change into a different lepton flavour β after propagating some
₁₇₅ distance. This phenomenon is called neutrino oscillation and requires that neutrinos
₁₇₆ must have a non-zero mass (as seen in subsection 1.2.1). This is direct evidence
₁₇₇ of beyond standard model physics. This behaviour has been characterised by the
₁₇₈ Pontecorvo-Maki-Nakagawa-Sakata (PMNS) [12–14] mixing matrix which describes
₁₇₉ how the flavour and mass of neutrinos are associated. This is analogous to the Cabibbo-
₁₈₀ Kobayashi-Maskawa (CKM) [15] matrix measured in quark physics.

₁₈₁ 1.2.1 Three Flavour Oscillations

₁₈₂ The PMNS parameterisation defines three flavour eigenstates, ν_e , ν_μ and ν_τ (indexed
₁₈₃ ν_α), which are assigned based upon the weak interaction flavour states and three mass
₁₈₄ eigenstates, ν_1 , ν_2 and ν_3 (indexed ν_i). Each mass eigenstate is the superposition of all
₁₈₅ three flavour states,

$$|\nu_i\rangle = \sum_\alpha U_{\alpha i} |\nu_\alpha\rangle. \quad (1.1)$$

₁₈₆ U is the PMNS matrix which correlates the mass and flavour eigenstates. Neutrinos
₁₈₇ interact with leptons of the same weak flavour eigenstate rather than mass eigenstate.

¹⁸⁸ The propagation of a neutrino flavour eigenstate, in a vacuum, can be re-written as a
¹⁸⁹ plane-wave solution to the time-dependent Schrödinger equation,

$$|\nu_\alpha(t)\rangle = \sum_i U_{\alpha i}^* |\nu_i\rangle e^{-i\phi_i}. \quad (1.2)$$

¹⁹⁰ The probability of observing a neutrino of flavour eigenstate β from one which
¹⁹¹ originated as flavour α can be calculated as,

$$P(\nu_\alpha \rightarrow \nu_\beta) = |\langle \nu_\beta | \nu_\alpha(t) \rangle|^2 = \sum_{i,j} U_{\alpha i}^* U_{\beta i} U_{\alpha j} U_{\beta j}^* e^{-i(\phi_j - \phi_i)} \quad (1.3)$$

¹⁹² The ϕ_i term can be expressed in terms of the energy, E_i , and magnitude of the
¹⁹³ three momenta, p_i , of the neutrino, $\phi_i = E_i t - p_i x$ (t and x being time and position
¹⁹⁴ coordinates). Therefore,

$$\phi_j - \phi_i = E_j t - E_i t - p_j x + p_i x. \quad (1.4)$$

¹⁹⁵ For a relativistic particle, $E_i \gg m_i$,

$$p_i = \sqrt{E_i^2 - m_i^2} \approx E_i - \frac{m_i^2}{2E_i}. \quad (1.5)$$

¹⁹⁶ Making the approximations that neutrinos are relativistic, the mass eigenstates
¹⁹⁷ were created with the same energy and that $x = L$, where L is the distance traveled by
¹⁹⁸ the neutrino, Equation 1.4 then becomes

$$\phi_j - \phi_i = \frac{\Delta m_{ij}^2 L}{2E}, \quad (1.6)$$

¹⁹⁹ where $\Delta m_{ij}^2 = m_j^2 - m_i^2$. This, teamed with further use of unitarity relations results
²⁰⁰ in Equation 1.3 becoming

$$P(\nu_\alpha \rightarrow \nu_\beta) = \delta_{\alpha\beta} - 4 \sum_{i>j} \Re \left(U_{\alpha i}^* U_{\beta i} U_{\alpha j} U_{\beta j}^* \right) \sin^2 \left(\frac{\Delta m_{ij}^2 L}{4E} \right) + (-) 2 \sum_{i>j} \Im \left(U_{\alpha i}^* U_{\beta i} U_{\alpha j} U_{\beta j}^* \right) \sin \left(\frac{\Delta m_{ij}^2 L}{2E} \right). \quad (1.7)$$

²⁰¹ Where $\delta_{\alpha\beta}$ is the Kronecker delta function and the negative sign is included for the
²⁰² oscillation probability of antineutrinos.

²⁰³ Typically, the PMNS matrix is parameterised into three mixing angles, a charge
²⁰⁴ parity (CP) violating phase δ_{CP} , and two Majorana phases $\alpha_{1,2}$,

$$U = \underbrace{\begin{pmatrix} 1 & 0 & 0 \\ 0 & c_{23} & s_{23} \\ 0 & -s_{23} & c_{23} \end{pmatrix}}_{\text{Atmospheric, Accelerator}} \underbrace{\begin{pmatrix} c_{13} & 0 & s_{13}e^{-i\delta_{CP}} \\ 0 & 1 & 0 \\ -s_{13}e^{-i\delta_{CP}} & 0 & c_{13} \end{pmatrix}}_{\text{Reactor, Accelerator}} \underbrace{\begin{pmatrix} c_{12} & s_{12} & 0 \\ -s_{12} & c_{12} & 0 \\ 0 & 0 & 1 \end{pmatrix}}_{\text{Reactor, Solar}} \underbrace{\begin{pmatrix} e^{i\alpha_1/2} & 0 & 0 \\ 0 & e^{i\alpha_2/2} & 0 \\ 0 & 0 & 1 \end{pmatrix}}_{\text{Majorana}}. \quad (1.8)$$

205 Where $s_{ij} = \sin(\theta_{ij})$ and $c_{ij} = \cos(\theta_{ij})$. The oscillation parameters are often
 206 grouped; (1, 2) as “solar”, (2, 3) as “atmospheric” and (1, 3) as “reactor”. Many
 207 neutrino experiments aim to measure the PMNS parameters from a wide array of
 208 origins, as is the purpose of this thesis.

209 The Majorana phase, $\alpha_{1,2}$, containing matrix included within Equation 1.8 is only
 210 included for completeness. For an oscillation analysis experiment, any term in this
 211 oscillation probability calculation containing this phase disappears due to taking the
 212 expectation value of the PMNS matrix.

213 A two flavour approximation can be attained when one assumes the third mass
 214 eigenstate is degenerate with another. As discussed in section 1.3, it is found that
 215 $\Delta m_{21}^2 \ll |\Delta m_{31}^2|$. This results in the two flavour approximation being reasonable for
 216 understanding the features of the oscillation. In this two flavour case, the mixing
 217 matrix becomes,

$$U_{2\text{ Flav.}} = \begin{pmatrix} \cos(\theta) & \sin(\theta) \\ -\sin(\theta) & \cos(\theta) \end{pmatrix}. \quad (1.9)$$

218 This culminates in the oscillation probability,

$$\begin{aligned} P(\nu_\alpha \rightarrow \nu_\alpha) &= 1 - \sin^2(2\theta) \sin^2\left(\frac{\Delta m^2 L}{4E}\right), \\ P(\nu_\alpha \rightarrow \nu_\beta) &= \sin^2(2\theta) \sin^2\left(\frac{\Delta m^2 L}{4E}\right). \end{aligned} \quad (1.10)$$

219 For $\alpha \neq \beta$. For a fixed neutrino energy, the oscillation probability is a sinusoidal
 220 function depending upon the distance over which the neutrino propagates. The

221 frequency and amplitude of oscillation are dependent upon the ratio of the $\Delta m^2 / 4E$
222 and $\sin^2 2\theta$, respectively. For more human-readable units, the maximum oscillation
223 probability for a fixed value of θ is given at $L[km] / E[GeV] \sim 1.27 / \Delta m^2$. It is this
224 calculation that determines the best L/E value for a given experiment to be designed
225 around for measurements of a specific value of Δm^2 .

226 1.2.2 The MSW Effect

227 The theory of neutrino oscillation in a vacuum is described in subsection 1.2.1. How-
228 ever, the beam neutrinos and atmospheric neutrinos originating from below the
229 horizon propagate through matter in the Earth. The coherent scattering of neutrinos
230 from a material target modifies the hamiltonian of the system. This results in a change
231 in the oscillation probability. Notably, charged current scattering ($\nu_e + e^- \rightarrow \nu_e + e^-$,
232 propagated by a W boson) only affects electron neutrinos compared to the neutral
233 current scattering ($\nu_l + l^- \rightarrow \nu_l + l^-$, propagated by a Z^0 boson), interacts through
234 all neutrino flavours equally. In the two-flavour limit, the effective mixing parameter
235 becomes

$$\sin^2(2\theta) \rightarrow \sin^2(2\theta_m) = \frac{\sin^2(2\theta)}{(A/\Delta m^2 - \cos(2\theta))^2 + \sin^2(2\theta)}, \quad (1.11)$$

236 where $A = 2\sqrt{2}G_F N_e E$ with N_e is the electron density of the medium and G_F is
237 Fermi's constant. It is clear to see that there exists a value of $A = \Delta m^2 \cos(2\theta)$ for
238 $\Delta m^2 > 0$ which results in a divergent mixing parameter. This resonance is due to
239 the Mikheyev-Smirnov-Wolfenstein (MSW) effect (or more colloquially, the matter
240 resonance) which regenerates the electron neutrino component of the neutrino flux
241 [16–18]. The density at which the resonance occurs is given by

$$N_e = \frac{\Delta m^2 \cos(2\theta)}{2\sqrt{2}G_F E}. \quad (1.12)$$

242 At densities lower than this critical value, the oscillation probability will be much
243 closer to that of vacuum oscillation. The resonance occurring from the MSW effect
244 depends on the sign of Δm^2 . Therefore, any neutrino oscillation experiment which
245 observes neutrinos and antineutrinos which have propagated through matter can have
246 some sensitivity to the ordering of the neutrino mass eigenstates.

247 For an experiment observing atmospheric neutrinos propagating through the Earth,
248 such as the studies presented in this thesis, a model of the Earth's density and layering
249 is required. The model used within this analysis is the Preliminary Reference Earth
250 Model (PREM) [19]. This model provides piecewise cubic polynomials. To follow the
251 methodology set in [20], this analysis simply approximates the model as four layers of
252 constant density with values taken from the PREM model, as described in Table 1.1.
253 As seen in [DB: Link to Oscillation chapter](#), the approximation in this methodology has
254 been removed and the density is instead integrated along the track using the piecewise
255 polynomials.

256 The density measurements provided in the PREM model are provided in terms
257 of mass density, whereas neutrino oscillations are sensitive to the electron number
258 density. This value can be computed as the product of the chemical composition and
259 mass density of each layer.

260 The beam oscillation probability in this thesis uses a baseline of 295km, density
261 2.6g/cm^3 , and chemical composition 0.5.

Layer	Outer Radius [km]	Density [g/cm ³]	Chemical composition (Z/A)
Inner Core	1220	13	0.468 ± 0.029
Outer Core	3480	11.3	0.468 ± 0.029
Lower Mantle	5701	5.0	0.497
Transition Zone	6371	3.3	0.497

Table 1.1: Description of the four layers of the Earth invoked within the PREM model [19].

262 1.3 Neutrino Oscillation Measurements

263 As evidence of beyond standard model physics, the 2015 Nobel Prize in Physics was
 264 awarded to the Super-Kamiokande (SK) [21] and Sudbury Neutrino Observatory
 265 (SNO) [22] collaborations for the first definitive observation of solar and atmospheric
 266 neutrino oscillation [23]. Since then, the field has seen a wide array of oscillation
 267 measurements from a variety of neutrino sources. As seen in subsection 1.2.1, the
 268 neutrino oscillation probability is dependent on the ratio of the propagation baseline, L ,
 269 to the neutrino energy, E . It is this ratio that determines the type of neutrino oscillation
 270 a particular experiment is sensitive to.

271 As illustrated in Figure 1.1, there are many neutrino sources that span a wide
 272 range of energies. The least energetic neutrinos are from diffuse supernovae and
 273 terrestrial neutrinos at $O(1)$ MeV whereas the most energetic neutrinos originate from
 274 atmospheric and galactic neutrinos of $> O(1)$ TeV.

275 1.3.1 Solar Neutrinos

276 Solar neutrinos are emitted from fusion reaction chains at the center of the Sun. The
 277 solar neutrino flux, given as a function of neutrino energy for different fusion and
 278 decay chains is illustrated in Figure 1.2. Whilst proton-proton fusion generates the
 279 largest flux of neutrinos, the neutrinos are of low energy and are difficult to reconstruct

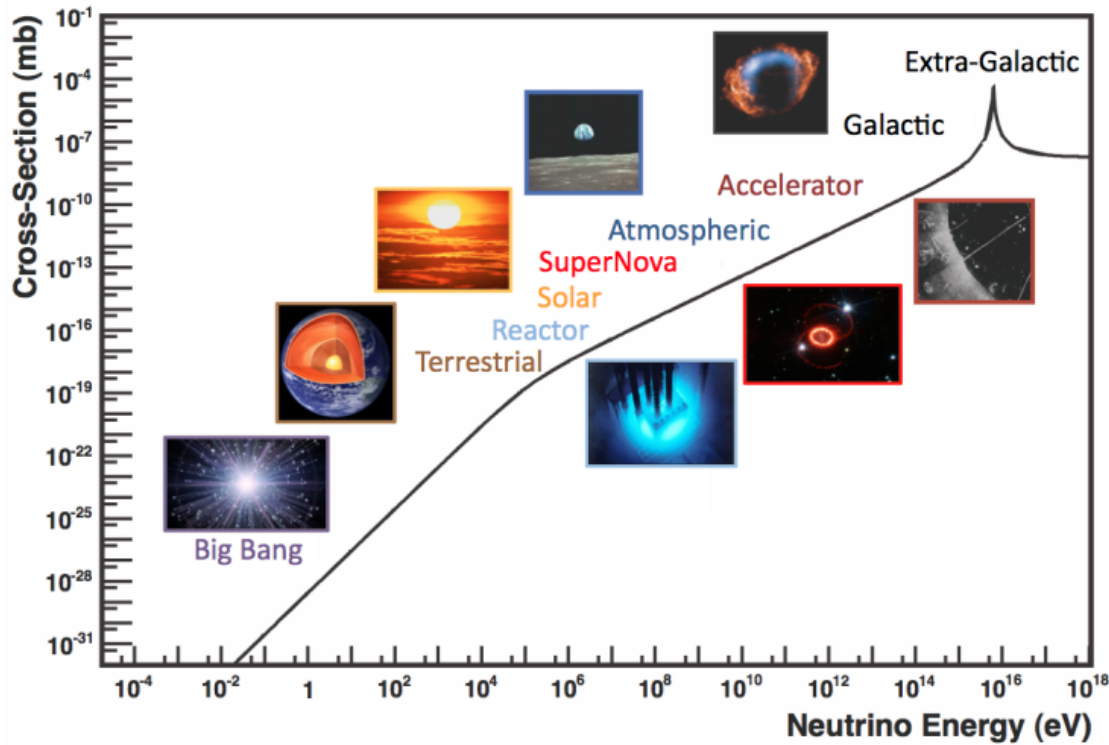


Figure 1.1: The cross-section of neutrinos from various natural and man-made sources as a function of neutrino energy. Taken from [24]

due to the IBD interaction threshold of 1.8MeV. Consequently, most experiments focus on the neutrinos from the decay of 8B (via ${}^8B \rightarrow {}^8Be^* + e^+ + \nu_e$), which are higher energy.

The first measurements of solar neutrinos observed a significant reduction in the event rate compared to predictions from the Standard Solar Model [26, 27]. The proposed solution to this “solar neutrino problem” was $\nu_e \leftrightarrow \nu_\mu$ oscillations in a precursory version of the PMNS model [28]. The Kamiokande [29], Gallex [30] and Sage [31] experiments confirmed the ~ 0.5 factor deficit of solar neutrinos.

The conclusive solution to this problem was determined by the SNO collaboration [32]. Using a deuterium water target to observe 8B neutrinos, the event rate of charged current (CC), neutral current (NC), and elastic scattering (ES) interactions (Given in Equation 1.13) was simultaneously measured. CC events can only occur for electron neutrinos, whereas the other interaction channels are agnostic to neutrino

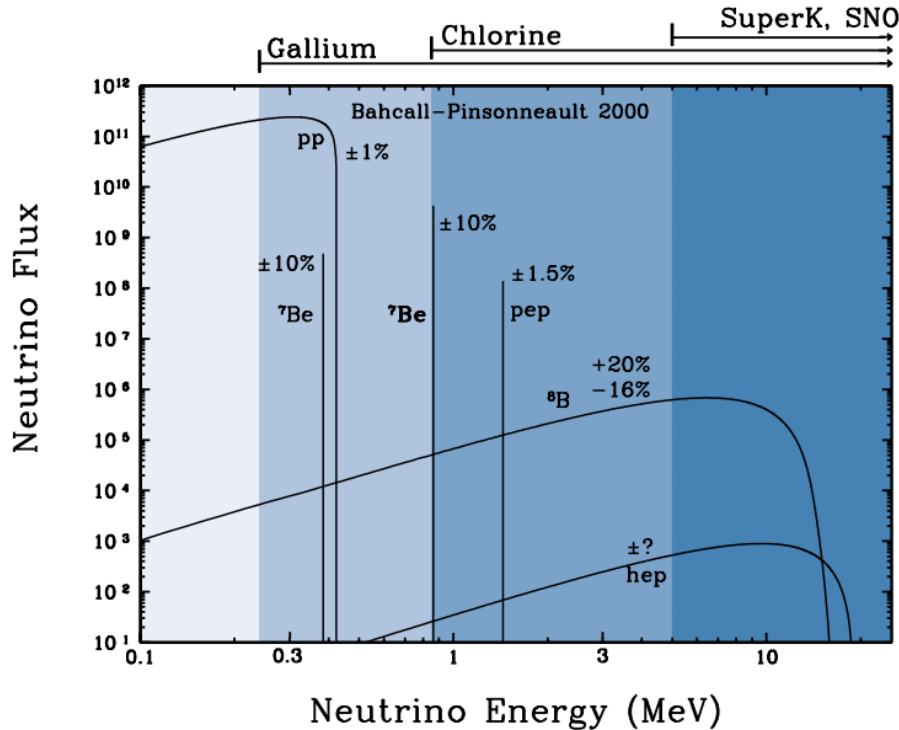


Figure 1.2: The solar neutrino flux as a function of neutrino energy for various fusion reactions and decay chains as predicted by the Standard Solar Model. Taken from [25].

flavour (Although the ES reaction is more sensitive to electron neutrino interactions). This meant that there were direct measurements of the ν_e and ν_x neutrino flux. It was concluded that the CC and ES interaction rates were consistent with the deficit previously observed. Most importantly, the NC reaction rate was only consistent with the others under the hypothesis of flavour transformation.

$$\begin{aligned}
 \nu_e + d &\rightarrow p + p + e^- & (\text{CC}) \\
 \nu_x + d &\rightarrow p + n + \nu_x & (\text{NC}) \\
 \nu_x + e^- &\rightarrow \nu_x + e^- & (\text{ES})
 \end{aligned} \tag{1.13}$$

Many experiments have since measured the neutrino flux of different interaction chains within the sun [33–35]. The most recent measurement was that of CNO neutr-

³⁰⁰ nos which were recently observed with 5σ significance by the Borexino collaboration.
³⁰¹ Future neutrino experiments aim to further these spectroscopic measurements of
³⁰² different fusion chains within the Sun [36–38]. Solar neutrinos act as an irreducible
³⁰³ background for dark matter experiments like DARWIN but oscillation parameter
³⁰⁴ measurements can be made [39].

³⁰⁵ 1.3.2 Atmospheric Neutrinos

³⁰⁶ The interactions of primary cosmic ray protons in Earth's upper atmosphere generate
³⁰⁷ showers of energetic hadrons. These are mostly pions and kaons which when they
³⁰⁸ decay produce a natural source of neutrinos spanning energies of MeV to TeV [40].
³⁰⁹ This decay is via

$$\begin{aligned} \pi^\pm &\rightarrow \mu^\pm + (\nu_\mu, \bar{\nu}_\mu) \\ \mu^\pm &\rightarrow e^\pm + (\nu_e, \bar{\nu}_e) + (\nu_\mu, \bar{\nu}_\mu) \end{aligned} \tag{1.14}$$

³¹⁰ such that for a single pion decay, three neutrinos are produced. The atmospheric
³¹¹ neutrino flux energy spectra as predicted by the Bartol [41], Honda [42, 43], and
³¹² FLUKA [44] models are illustrated in Figure 1.3. The flux distribution peaks at an
³¹³ energy of $O(10)\text{GeV}$. The uncertainties associated with these models are dominated
³¹⁴ by the hadronic production of kaon and pions as well as the primary cosmic flux.

³¹⁵ Unlike long-baseline experiments which have a fixed baseline, the distance at-
³¹⁶ mospheric neutrinos propagate is dependent upon the zenith angle at which they
³¹⁷ interact. This is illustrated in Figure 1.4. Neutrinos that are generated directly above
³¹⁸ the detector ($\cos(\theta) = 1.0$) have a baseline equivalent to the height of the atmosphere
³¹⁹ whereas neutrinos that interact directly below the detector ($\cos(\theta) = -1.0$) have to

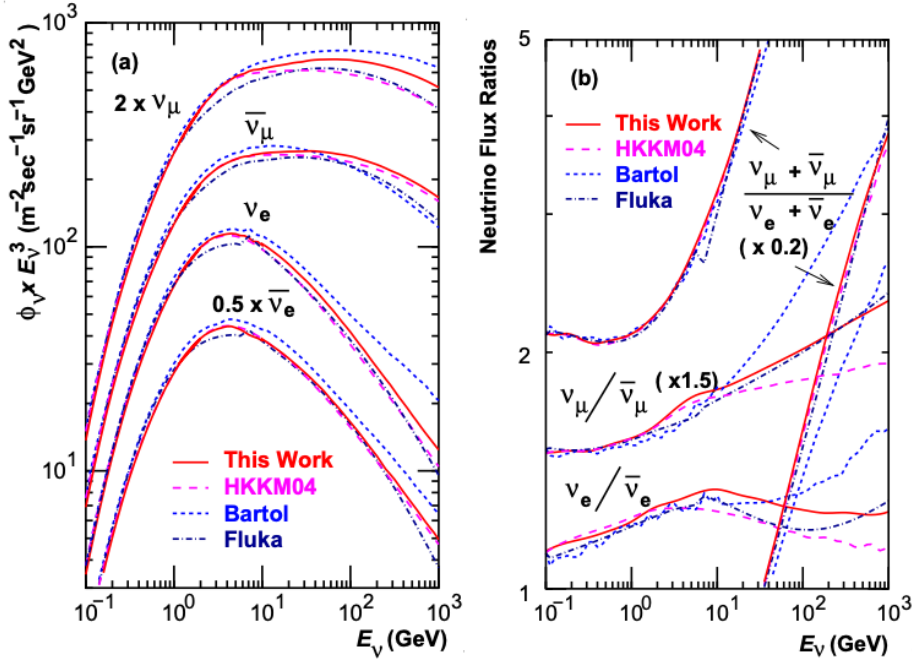


Figure 1.3: Left panel: The atmospheric neutrino flux for different neutrino flavours as a function of neutrino energy as predicted by the 2007 Honda model (“This work”) [42], the 2004 Honda model (“HKKM04”) [43], the Bartol model [41] and the FLUKA model [44]. Right panel: The ratio of the muon to electron neutrino flux as predicted by all the quoted models. Both figures taken from [42].

travel a length equal to the diameter of the Earth. This means atmospheric neutrinos have a baseline that varies from $O(20)\text{km}$ to $O(6 \times 10^3)\text{km}$. Any neutrino generated at or below the horizon will be subject to matter effects as they propagate through the Earth.

Figure 1.5 highlights the neutrino flux as a function of the zenith angle for different slices of neutrino energy. For medium to high-energy neutrinos (and to a lesser degree for low-energy neutrinos), the flux is approximately symmetric around $\cos(\theta) = 0$. To the accuracy of this approximation, the systematic uncertainties associated with atmospheric flux for comparing upward-going and down-going neutrino cancels. This allows the down-going events, which are mostly insensitive to oscillation probabilities, to act as an unoscillated prediction (similar to a near detector in an accelerator neutrino experiment).

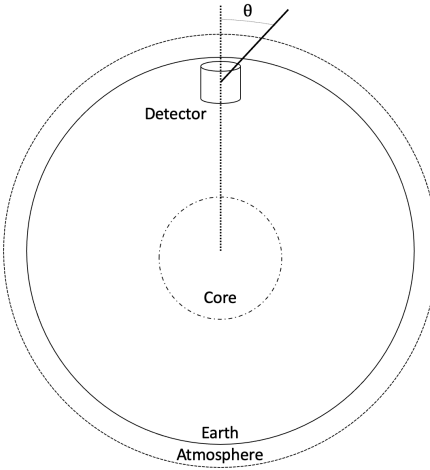


Figure 1.4: A diagram illustrating the definition of zenith angle as used in the Super Kamiokande experiment [45].

Precursory hints of atmospheric neutrinos were observed in the mid-1960s search-

ing for $\nu_\mu^{(-)} + X \rightarrow X^* + \mu^\pm$ [46]. This was succeeded with the IMB-3 [47] and

Kamiokande [48] experiments which measured the ratio of muon neutrinos com-

pared to electron neutrinos $R(\nu_\mu/\nu_e)$. Both experiments were found to have a con-

sistent deficit of muon neutrinos, with $R(\nu_\mu/\nu_e) = 0.67 \pm 0.17$ and $R(\nu_\mu/\nu_e) =$

$0.60^{+0.07}_{-0.06} \pm 0.05$. Super-Kamiokande (SK) [45] extended this analysis by fitting os-

cillation parameters in $P(\nu_\mu \rightarrow \nu_\tau)$ which found best fit parameters $\sin^2(2\theta) > 0.92$

and $1.5 \times 10^{-3} < \Delta m^2 < 3.4 \times 10^{-3} \text{ eV}^2$.

Since then, atmospheric neutrino experiments have been making precision mea-

surements of the $\sin^2(\theta_{23})$ and Δm^2_{32} oscillation parameters. Atmospheric neutrino

oscillation is dominated by $P(\nu_\mu \rightarrow \nu_\tau)$, where SK observed a 4.6σ discovery of ν_τ

appearance [49]. Figure 1.6 illustrates the current estimates on the atmospheric mixing

parameters from a wide range of atmospheric and accelerator neutrino observatories.

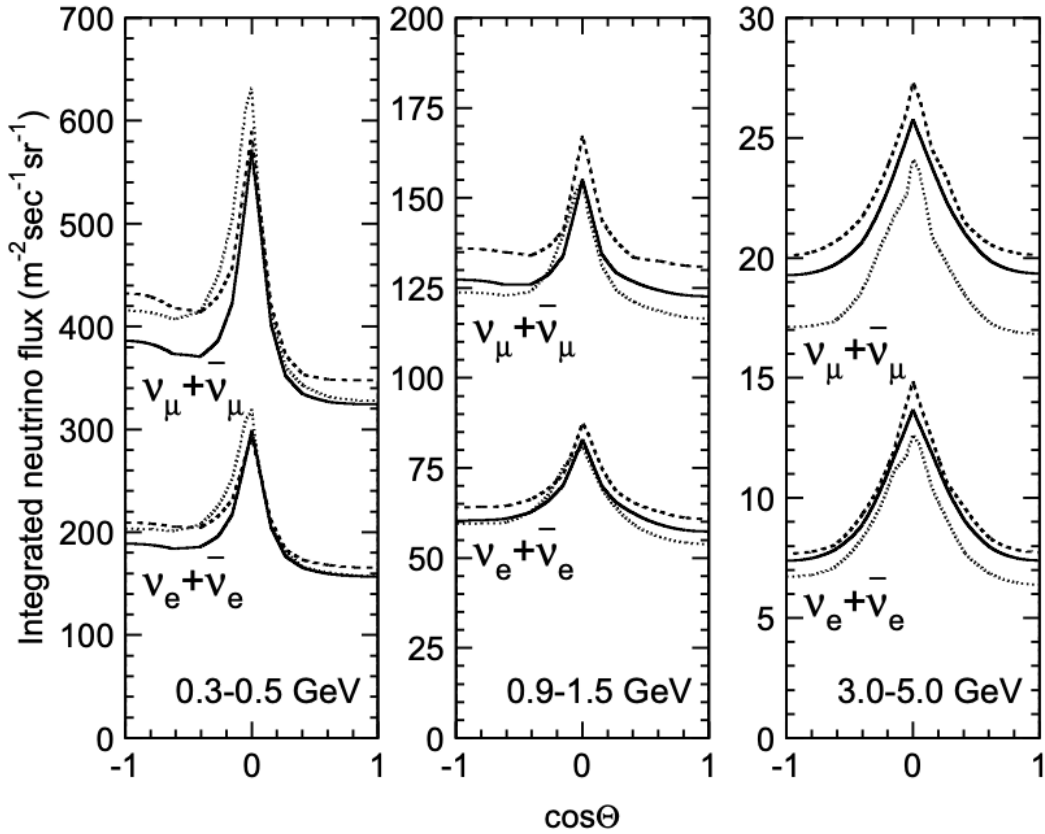


Figure 1.5: Predictions of the summed neutrino and antineutrino flux for electron and muon neutrinos from the Bartol [41], Honda [42] and FLUKA [44] models as a function of zenith angle with respect to the detector. Left panel: $0.3 < E_\nu < 0.5$. Middle panel: $0.9 < E_\nu < 1.5$. Right panel: $3.0 < E_\nu < 5.0$. Figures taken from [45].

345 1.3.3 Accelerator Neutrinos

346 The concept of using a man-made “neutrino beam” was first realised in 1962 [56].
 347 Since then, many experiments have followed which all use the same fundamental
 348 concepts. Typically, a proton beam is aimed at a target producing charged mesons that
 349 decay to neutrinos. The mesons can be sign-selected by the use of magnetic focusing
 350 horns to generate a neutrino or antineutrino beam. Pions are the primary meson that
 351 decay and depending on the orientation of the magnetic field, a muon (anti-)neutrino
 352 beam is generated via $\pi^+ \rightarrow \mu^+ + \nu_\mu$ or $\pi^- \rightarrow \mu^- + \bar{\nu}_\mu$. The decay of muons and
 353 kaons does result in an irreducible intrinsic electron neutrino background. In T2K,

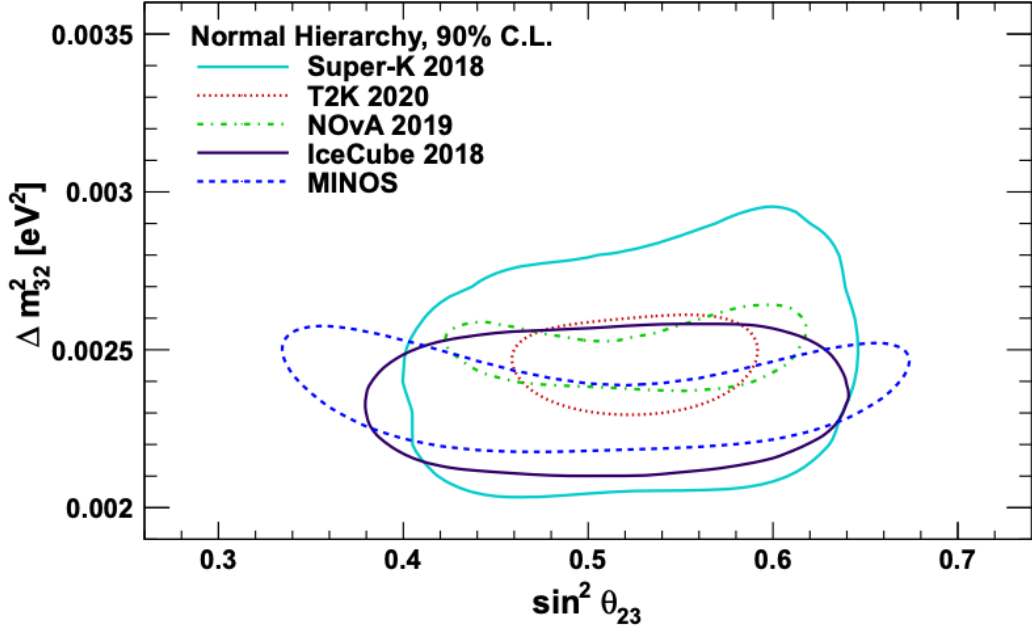


Figure 1.6: Constraints on the atmospheric oscillation parameters, $\sin^2(\theta_{23})$ and Δm_{32}^2 , from atmospheric and long baseline experiments: SK [50], T2K [51], NOvA [52], IceCube [53] and MINOS [54]. Figure taken from [55].

354 this background contamination is $O(< 1\%)$ [57]. There is also an approximately $\sim 5\%$
 355 “wrong-sign” neutrino background of $\bar{\nu}_\mu$ generated via the same decays.

356 The energy of each neutrino in the beam is dependent on the energy of the initial
 357 proton beam. Therefore, tuning the proton energy allows the neutrino energy to be set
 358 to a value that maximises the disappearance oscillation probability in the L/E term in
 359 Equation 1.10. This means that accelerator experiments are typically more sensitive
 360 to the mixing parameters as compared to a natural neutrino source. However, the
 361 disadvantage compared to atmospheric neutrino experiments is that the baseline has
 362 to be shorter due to the lower flux. Consequently, there is typically less sensitivity to
 363 matter effects and the ordering of the neutrino mass eigenstates.

364 A neutrino experiment measures

$$R(\vec{x}) = \Phi(E_\nu) \times \sigma(E_\nu) \times \epsilon(\vec{x}) \times P(\nu_\alpha \rightarrow \nu_\beta), \quad (1.15)$$

where $R(\vec{x})$ is the event rate of neutrinos at position \vec{x} , $\Phi(E_\nu)$ is the flux of neutrinos with energy E_ν , $\sigma(E_\nu)$ is the cross-section of the neutrino interaction and $\epsilon(\vec{x})$ is the efficiency of the detector. In order to leverage the most out of an accelerator neutrino experiment, the flux and cross-section systematics need to be constrained. This is typically done via the use of a “near detector”, situated at a baseline of $O(1)$ km. This detector observes the unoscillated neutrino flux and constrains the parameters used within the flux and cross-section model.

The first accelerator experiments to precisely measure oscillation parameters were MINOS [58] and K2K [59]. These experiments confirmed the $\nu_\mu \rightarrow \nu_\mu$ oscillations seen in atmospheric neutrino experiments by finding consistent mixing parameter values for $\sin^2(\theta_{23})$ and Δm_{23}^2 . The current generation of accelerator neutrino experiments, T2K and NOvAextended this field by observing $\bar{\nu}_\mu \rightarrow \bar{\nu}_e$ and lead the sensitivity to atmospheric mixing parameters as seen in Figure 1.6 [60]. The two experiments differ in their peak neutrino energy, baseline, and detection technique. The NOvAexperiment is situated at a baseline of 810km from the NuMI beamline which delivers 2GeV neutrinos. The T2K neutrino beam is peaked around 0.6GeV and propagates 295km. The NOvAexperiment also uses functionally identical detectors (near and far) which allow the approximate cancellation of detector systematics whereas T2K uses a plastic scintillator technique at the near detector and a water Cherenkov far detector. The future generation experiments DUNE [61] and Hyper-Kamiokande [62] will succeed these experiments as the high-precision era of neutrino oscillation parameter measurements develops.

³⁸⁷ Several anomalous results have been observed in the LSND [9] and MiniBooNE [10]
³⁸⁸ detectors which were designed with purposefully short baselines. Parts of the neu-
³⁸⁹ trino community attributed these results to oscillations induced by a fourth “sterile”
³⁹⁰ neutrino [63] but several searches in other experiments, MicroBooNE [64] and KAR-
³⁹¹ MEN [65], found no hints of additional neutrino species. The solution to the anomalous
³⁹² results are still being determined.

³⁹³ 1.3.4 Reactor Neutrinos

³⁹⁴ As illustrated in the first discovery of neutrinos (section 1.1), nuclear reactors are a very
³⁹⁵ useful man-made source of electron antineutrinos. For reactors that use low-enriched
³⁹⁶ uranium ^{235}U as fuel, the antineutrino flux is dominated by the β -decay fission of ^{235}U ,
³⁹⁷ ^{238}U , ^{239}Pu and ^{241}Pu [66] as illustrated in Figure 1.7.

³⁹⁸ Due to their low energy, reactor electron antineutrinos predominantly interact
³⁹⁹ via the inverse β -decay (IBD) interaction. The typical signature contains two signals
⁴⁰⁰ delayed by $O(200)\mu\text{s}$; firstly the prompt photons from positron annihilation, and
⁴⁰¹ secondly the photons emitted ($E_{tot}^\gamma = 2.2\text{MeV}$) from de-excitation after neutron capture
⁴⁰² on hydrogen. Searching for both signals improves the detector’s ability to distinguish
⁴⁰³ between background and signal events [68]. Recently, SK included gadolinium dopants
⁴⁰⁴ into the ultra-pure water to increase the energy released from the photon cascade to
⁴⁰⁵ $\sim 8\text{MeV}$ and reduce the time of the delayed signal to $\sim 28\mu\text{s}$.

⁴⁰⁶ There are many short baseline experiments ($L \sim O(1)\text{km}$) that have measured the
⁴⁰⁷ $\sin^2(\theta_{13})$ and Δm_{23}^2 oscillation parameters. Daya Bay [69], RENO [70] and Double
⁴⁰⁸ Chooz [71] have all provided precise measurements, with the first discovery of a
⁴⁰⁹ non-zero θ_{13} made by Daya Bay and RENO (and complimented by T2K [71]). The
⁴¹⁰ constraints on $\sin^2(\theta_{13})$ by the reactor experiments lead the field and are often used as

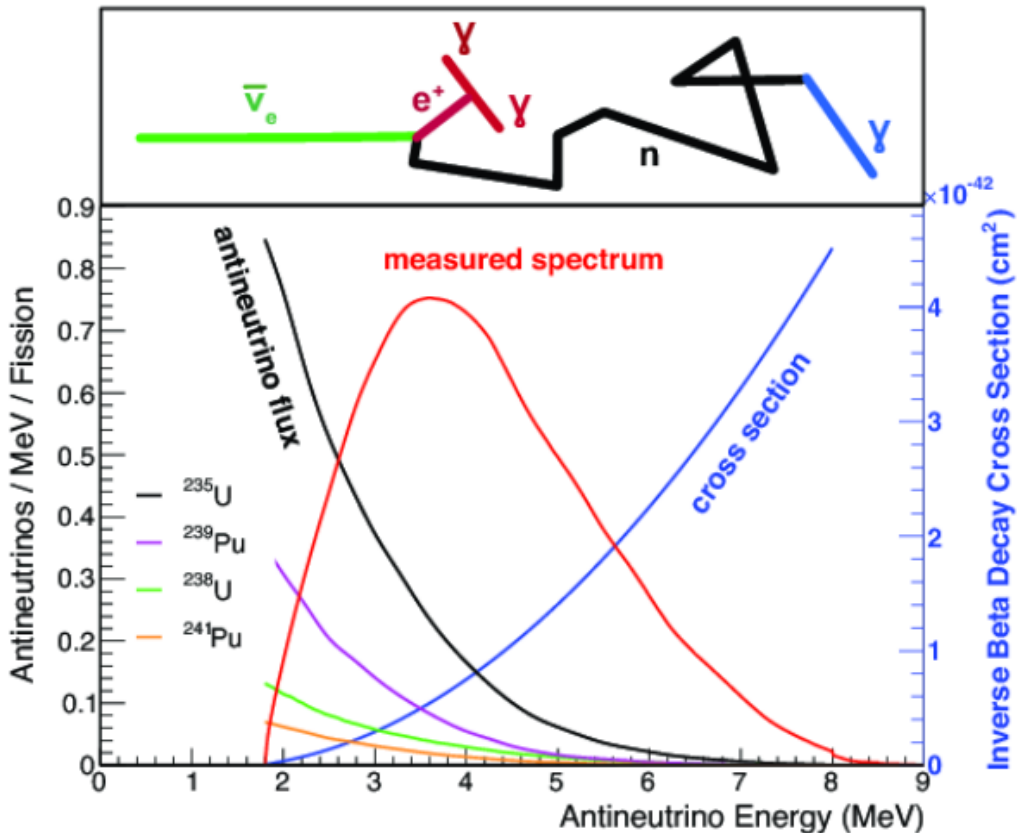


Figure 1.7: Reactor electron antineutrino fluxes for ^{235}U (Black), ^{238}U (Green), ^{239}Pu (Purple), and ^{241}Pu (Orange) isotopes. The inverse β -decay cross-section (Blue) and corresponding measurable neutrino spectrum (Red) are also given. Top panel: Schematic of Inverse β -decay interaction including the eventual capture of the emitted neutron. This capture emits a γ -ray which provides a second signal of the event. Taken from [67].

411 external inputs to accelerator neutrino experiments to improve their sensitivity to δ_{CP}
 412 and mass hierarchy determination. JUNO-TAO [72], a small collaboration within the
 413 larger JUNO experiment, is a next-generation reactor experiment that aims to precisely
 414 measure the isotopic antineutrino yields from the different fission chains. Alongside
 415 this, it aims to explain the ‘5MeV excess’ [73–75] by conducting a search for sterile
 416 neutrinos with a mass scale of around 1eV.

417 Kamland [76] is the only experiment to have observed reactor neutrinos using a
 418 long baseline (flux weighted averaged baseline of $L \sim 180\text{km}$) which allows it to have
 419 sensitivity to Δm_{12}^2 . Combined with the SK solar neutrino experiment, the combined

⁴²⁰ analysis puts the most stringent constraint on Δm_{12}^2 [77] which is used as a prior
⁴²¹ uncertainty within accelerator neutrino experiments.

⁴²² **Chapter 2**

⁴²³ **T2K and SK Experiment Overview**

⁴²⁴ As the successor of the Kamiokande experiment, the Super-Kamiokande (SK) collaboration has been leading atmospheric neutrino oscillation analyses for over two decades.
⁴²⁵ The detector has provided some of the strongest constraints on proton decay limits
⁴²⁶ and as well as the first precise measurements of the Δm_{23}^2 and $\sin^2(\theta_{23})$ neutrino
⁴²⁷ oscillation parameters. Despite this, the ability of the detector to low-energy neutrino
⁴²⁸ events has been significantly improved with the recent gadolinium doping of the
⁴²⁹ ultra-pure water target. section 2.1 describes the history, detection technique, and
⁴³⁰ operation of the SK detector.

⁴³² The Tokai-to-Kamioka (T2K) experiment was one of the first long-baseline experiments to use both neutrino and antineutrino beams to precisely measure the
⁴³³ charge parity violation within the neutrino sector. With the SK detector observing
⁴³⁴ the oscillated neutrino flux, the T2K experiment observed the first hints of a non-zero
⁴³⁵ $\sin^2(\theta_{13})$ measurement and continues to lead the field with the constraints it pro-
⁴³⁶ vides on $\sin^2(\theta_{13})$, $\sin^2(\theta_{23})$, Δm_{23}^2 and δ_{CP} . section 2.2 documents the techniques
⁴³⁷ which T2K uses in generating its neutrino beam as well as the ‘near-detector’ used to
⁴³⁸ constrain the flux and cross-section parameters invoked within the systematic models.

⁴⁴⁰ **2.1 The Super-Kamiokande Experiment**

⁴⁴¹ The SK experiment began taking data in 1996 [78] and has had many modifications
⁴⁴² throughout its lifespan. There have been seven defined periods of data taking as

noted in Table 2.1. Data taking began in SK-I which ran for five years. Between the SK-I and SK-II periods, a significant proportion of the PMTs were damaged during maintenance. Those that survived were equally distributed throughout the detector in the SK-II era, which resulted in a reduced photo-coverage. From SK-III onwards, repairs to the detector meant the full suite of PMTs was operational. Before the start of SK-IV, the data acquisition and electronic systems were upgraded. Between SK-IV and SK-V, a significant effort was placed into tank open maintenance and repair/replacement of defective PMTs, a task for which the author of this thesis was required. Consequently, the detector conditions were significantly different between the two operational periods. SK-VI saw the start of the 0.01% gadolinium doped water. SK-VII, which started during the writing of this thesis, has increased the gadolinium concentration to 0.03% for continued operation. [DB: Link to Linyan's talk from Nu2022.](#)

Period	Start Date	End Date	Live-time (days)
I	April 1996	July 2001	1489.19
II	October 2002	October 2005	798.59
III	July 2006	September 2008	518.08
IV	September 2008	May 2018	3244.4
V	January 2019	July 2020	461.02
VI	July 2020	May 2022	583.3
VII	May 2022	Ongoing	N/A

Table 2.1: The various SK periods and respective live-time. The SK-VI live-time is calculated until 1st April 2022. SK-VII started during the writing of this thesis.

2.1.1 The SK Detector

The basic structure of the Super-Kamiokande (SK) detector is a cylindrical tank with a diameter 39.3m and height 41.1m filled with ultrapure water [79]. A diagram of the significant components of the SK detector is illustrated in Figure 2.1. The SK detector

is situated in the Kamioka mine in Gifu, Japan. The mine is underground with roughly 1km rock overburden (2.7km water equivalent overburden) [80]. At this depth, the rate of cosmic ray muons is significantly decreased to a value of $\sim 2\text{Hz}$. The top of the tank is covered with stainless steel which is designed as a working platform for maintenance, calibration, and location for high voltage and data acquisition electronics.

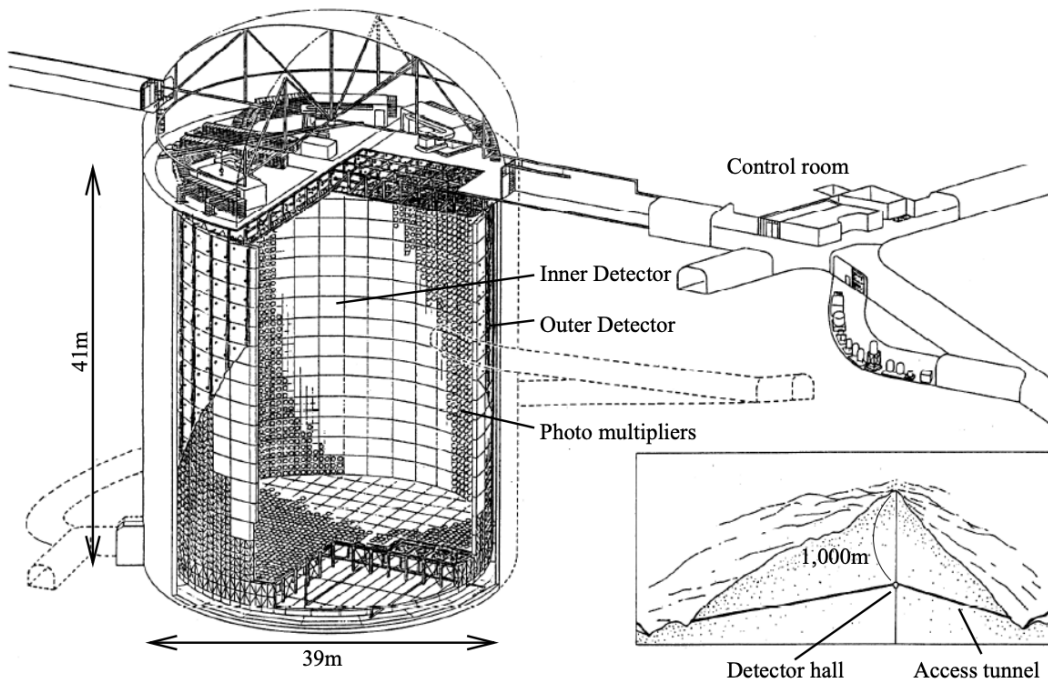


Figure 2.1: A schematic diagram of the Super-Kamiokande Detector. Taken from [81].

A smaller cylindrical structure (36.2m diameter, 33.8m height) is situated inside the tank, with an approximate 2m gap between this structure and the outer tank wall. The purpose of this structure is to support the photomultiplier tubes (PMTs). The volume inside and outside the support structure is referred to as the inner detector (ID) and outer detector (OD), respectively. In the SK-IV era, the ID and OD are instrumented by 11,129 50cm and 1,885 20cm PMTs respectively [79]. The ID contains a 32kton mass of water. Many analyses performed at SK use a “fiducial volume” defined by the volume of water inside the ID excluding some distance to the ID wall. This reduces the volume of the detector which is sensitive to neutrino events but reduces radioactive

⁴⁷⁴ backgrounds and allows for better reconstruction performance. The nominal fiducial
⁴⁷⁵ volume is defined as the area contained inside 2m from the ID wall for a total of
⁴⁷⁶ 22.5kton water [82].

⁴⁷⁷ The two regions of the detector (ID and OD) are optically separated with opaque
⁴⁷⁸ black plastic. The purpose of this is to determine whether a track entered or exited
⁴⁷⁹ the ID. This allows cosmic ray muons and partially contained events to be tagged and
⁴⁸⁰ separated from neutrino events entirely contained within the ID. This black plastic is
⁴⁸¹ also used to cover the area between the ID PMTs to reduce photon reflection from the
⁴⁸² ID walls. Opposite to this, the OD is lined with a reflective material to allow photons to
⁴⁸³ reflect around inside the OD until collected by one of the PMTs. Furthermore, each OD
⁴⁸⁴ PMT is backed with $50 \times 50\text{cm}$ plates of wavelength shifting acrylic which increases
⁴⁸⁵ the efficiency of light collection [80].

⁴⁸⁶ In the SK-IV data-taking period, the photocathode coverage of the detector, or the
⁴⁸⁷ fraction of the ID wall instrumented with PMTs, is $\sim 40\%$ [80]. The PMTs have a
⁴⁸⁸ quantum efficiency (the ratio of detected electrons to incident photons) of $\sim 21\%$ for
⁴⁸⁹ photons with wavelengths of $360\text{nm} < \lambda < 390\text{nm}$. The proportion of photoelectrons
⁴⁹⁰ that produce a signal in the dynode of a PMT, termed the collection efficiency, is
⁴⁹¹ $> 70\%$ [80]. The PMTs used within SK are most sensitive to photons with wavelength
⁴⁹² $300\text{nm} \leq \lambda \leq 600\text{nm}$ [80]. One disadvantage of using PMTs as the detection media
⁴⁹³ is that the Earth's geomagnetic field can modify its response. Therefore, a set of
⁴⁹⁴ compensation coils is built around the inner surface of the detector to mitigate this
⁴⁹⁵ effect [83].

⁴⁹⁶ As mentioned, the SK detector is filled with ultrapure water, which in a perfect
⁴⁹⁷ world would contain no impurities. However, bacteria and organic compounds can
⁴⁹⁸ significantly degrade the water quality. This decreases the attenuation length which
⁴⁹⁹ reduces the total number of photons that hit a PMT. To combat this, a sophisticated

500 water treatment system has been developed [80, 84]. UV lights, mechanical filters, and
501 membrane degasifiers are used to reduce the bacteria, suspended particulates, and
502 radioactive materials from the water. The flow of water within the tank is also critical
503 as it can remove stagnant bacterial growth or build-up of dust on the surfaces within
504 the tank. Gravity drifts impurities in the water towards the bottom of the tank which,
505 if left uncontrolled, can create asymmetric water conditions between the top and
506 bottom of the tank. Typically, the water entering the tank is cooled below the ambient
507 temperature of the tank to control convection and inhibit bacteria growth. Furthermore,
508 the dark noise hits within PMTs is sensitive to the PMT temperature [85] so controlling
509 the temperature gradients within the tank is beneficial for stable measurements.

510 SK-VI is the first phase of the SK experiment to use gadolinium dopants within
511 the ultrapure water [DB: Link to Linyan's talk at Nu2022](#). As such, the SK water
512 system had to be replaced to avoid removing the gadolinium concentrate from the
513 ultrapure water [86]. For an inverse β -decay (IBD) interaction in a water target, the
514 emitted neutron is thermally captured on hydrogen. This process releases 2.2MeV γ
515 rays which are difficult to detect due to Compton scattered electrons from a γ ray of
516 this energy is very close to the Cherenkov threshold, limiting the number of photons
517 produced. Thermal capture of neutrons on gadolinium generates γ rays with higher
518 energy meaning they are more easily detected. SK-VI has 0.01% Gd loading (0.02%
519 gadolinium sulphate by mass) which causes \approx 50% of neutrons emitted by IBD to
520 be captured on gadolinium [87, 88]. Whilst predominantly useful for low energy
521 analyses, Gd loading allows better $\nu/\bar{\nu}$ separation for atmospheric neutrino event
522 selections [89]. Efforts are currently in place to increase the gadolinium concentrate to
523 0.03% for \approx 75% neutron capture efficiency on gadolinium [DB: Link to Mark's talk at](#)
524 [Nu2022](#). The final stage of loading targets 0.1% concentrate.

525 2.1.2 Calibration

526 The calibration of the SK detector is documented in [79] and summarised below. The
527 analysis presented within this thesis is dependent upon ‘high energy events’ (Charged
528 particles with $O(> 100)\text{MeV}$ momenta). These are events that are expected to generate
529 a larger number of photons such that each PMT will be hit with multiple photons.
530 The reconstruction of these events depends upon the charge deposited within each
531 PMT and the timing response of each individual PMT. Therefore, the most relevant
532 calibration techniques to this thesis are outlined.

533 Before installation, 420 PMTs were calibrated to have identical charge responses
534 and then distributed throughout the tank in a cross-shape pattern (As illustrated by
535 Figure 2.2). These are used as a standardised measure for the rest of the PMTs installed
536 at similar geometric positions within SK to be calibrated against. To perform this
537 calibration, a xenon lamp is located at the center of the SK tank which flashes uniform
538 light at 1Hz. This allows for geometrical effects, water quality variation, and timing
539 effects to be measured in-situ throughout normal data-taking periods.

540 When specifically performing calibration of the detector (in out-of-data taking
541 mode), the water in the tank was circulated to avoid top/bottom asymmetric water
542 quality. Any non-uniformity within the tank significantly affects the PMT hit proba-
543 bility through scattering or absorption. This becomes a dominant effect for the very
544 low-intensity light sources discussed later which are designed such that only one
545 photon is incident upon a given PMT.

546 The “gain” of a PMT is defined as the ratio of the total charge of the signal produced
547 compared to the charge of photoelectrons emitted by the photocathodes within the
548 PMT. To calibrate the signal of each PMT, the “relative” and “absolute” gain values are

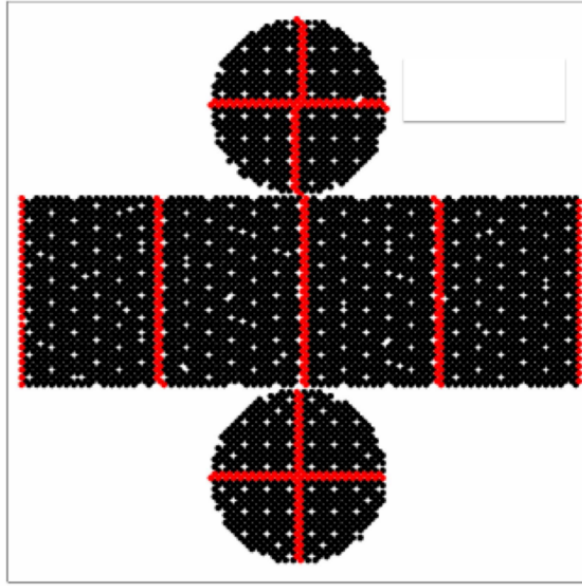


Figure 2.2: The location of “standard PMTs” (red) inside the SK detector. Taken from [79].

549 measured. The relative gain is the variation of gain among each of the PMTs whereas
 550 the absolute gain is the average gain of all PMTs.

551 The relative gain is calibrated as follows. A laser is used to generate two measure-
 552 ments; a high-intensity flash that illuminates every PMT with a sufficient number of
 553 photons, and a low-intensity flash in which only a small number of PMTs collect light.
 554 The first measurement creates an average charge, $Q_{obs}(i)$ on PMT i , whereas the second
 555 measurement ensures that each hit PMT only generates a single photoelectron. For the
 556 low-intensity measurement, the number of times each PMT records a charge larger
 557 than 1/4 photoelectrons, $N_{obs}(i)$, is counted. The values measured can be expressed as

$$\begin{aligned} Q_{obs}(i) &\propto I_H \times f(i) \times \epsilon(i) \times G(i), \\ N_{obs}(i) &\propto I_L \times f(i) \times \epsilon(i), \end{aligned} \tag{2.1}$$

558 Where I_H and I_L is the intensity of the high and low flashes, $f(i)$ is the acceptance
 559 efficiency of the i^{th} PMT, $\epsilon(i)$ is the product of the quantum and collection efficiency

560 of the i^{th} PMT and $G(i)$ is the gain of the i^{th} PMT. The relative gain for each PMT can
 561 determined by taking the ratio of these quantities.

562 The absolute gain calibration is performed by observing fixed energy γ -rays of
 563 $E_{\gamma} \sim 9\text{MeV}$ emitted isotropically from neutron capture on a NiCf source situated at
 564 the center of the detector. This generates a photon yield of about 0.004 photoelec-
 565 trons/PMT/event, meaning that $> 99\%$ of PMT signals are generated from single
 566 photoelectrons. A charge distribution is generated by performing this calibration over
 567 all PMTs, and the average value of this distribution is taken to be the absolute gain
 568 value.

569 As mentioned in subsection 2.1.1, the average quantum and collection efficiency
 570 for the SK detector is $\sim 21\%$ and $> 70\%$ respectively. However, these values do differ
 571 between each PMT and need to be calibrated accordingly. Consequently, the NiCf
 572 source is also used to calibrate the “quantum \times collection” efficiency (denoted “QE”)
 573 value of each PMT. The NiCf low-intensity source is used as the PMT hit probability
 574 is proportional to the QE ($N_{\text{obs}}(i) \propto \epsilon(i)$ in Equation 2.1). A Monte Carlo prediction
 575 which includes photon absorption, scattering, and reflection is made to estimate the
 576 number of photons incident on each PMT and the ratio of the number of predicted
 577 to observed hits is calculated. The difference is attributed to the QE efficiency of that
 578 PMT. This technique is extended to calculate the relative QE efficiency by normalizing
 579 the average of all PMTs which removes the dependence on the light intensity.

580 Due to differing cable lengths and readout electronics, the timing response between
 581 a photon hitting the PMT and the signal being captured by the data acquisition can be
 582 different between each PMT. Due to threshold triggers (Described in subsection 2.1.3),
 583 the time at which a pulse reaches a threshold is dependent upon the size of the pulse.
 584 This is known as the ‘time-walk’ effect and also needs to be accounted for in each PMT.
 585 To calibrate the timing response, a pulse of light with width 0.2ns is emitted into the

586 detector through a diffuser Two-dimensional distributions of time and pulse height
587 (or charge) are made for each PMT and are used to calibrate the timing response. This
588 is performed in-situ whilst data taking with the light source pulsing at 0.03Hz.

589 The top/bottom water quality asymmetry is measured using the NiCf calibration
590 data and cross-referencing these results to the “standard PMTs”. The water attenuation
591 length is continuously measured by the rate of vertically-downgoing cosmic-ray
592 muons which enter via the top of the tank.

593 2.1.3 Data Acquisition and Triggering

594 Dark noise is the phenomenon where a PMT registers a pulse that is consistent with a
595 single photoelectron emitted from photon detection despite the PMT being in complete
596 darkness. This is predominately caused by two processes. Firstly there is intrinsic
597 dark noise which is where photoelectrons gain enough thermal energy to be emitted
598 from the photocathode, and secondly, the radioactive decay of contaminants inside the
599 structure of the PMT. Typical dark noise rate for PMTs used within SK are $O(3)$ kHz [80]
600 which equates to about 12 dark noise hits per 220ns [90]. This is lower than the
601 expected number of photons generated for a ‘high energy event’ (As described in
602 subsection 2.1.4) but instability in this value can cause biases in reconstruction.

603 The analysis presented in this thesis only uses the SK-IV period of the SK exper-
604 iment so this subsection focuses on the relevant points of the data acquisition and
605 triggering systems to that SK period. The earlier data acquisition and triggering
606 systems are documented in [91, 92].

607 Before the SK-IV period started, the existing front-end electronics were replaced
608 with “QTC-Based Electrons with Ethernet, QBEE” systems [93]. When the QBEE
609 observes a signal above a 1/4 photoelectron threshold, the charge-to-time (QTC)

converter generates a rectangular pulse. The start of the rectangular pulse indicates the time at which the analog photoelectron signal was received and the width of the pulse indicates the total charge integrated throughout the signal. This is then digitized by time-to-digital converters and sent to the “front-end” PCs. The digitized signal from every QBEE is then chronologically ordered and sent to the “merger” PCs. It is the merger PCs that apply the software trigger. Any triggered events are passed to the “organizer” PC. This sorts the data stream of multiple merger PCs into chronologically ordered events which are then saved to disk. The schematic of data flow from PMTs to disk is illustrated in Figure 2.3.

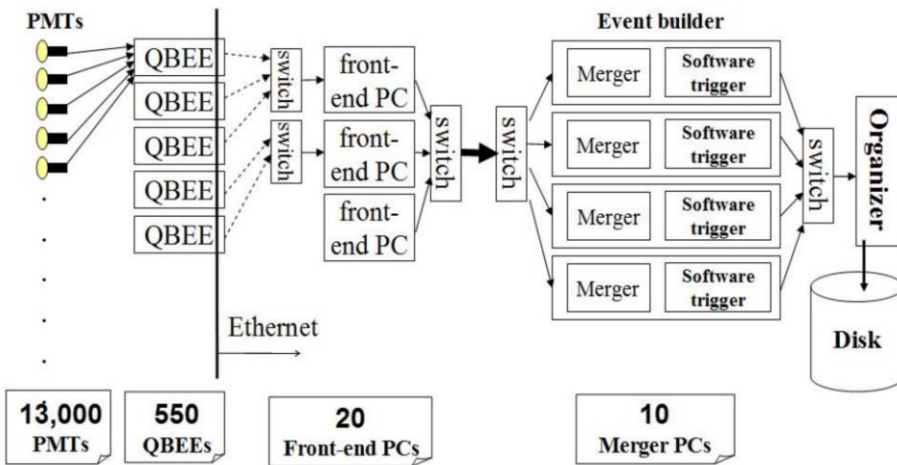


Figure 2.3: Schematic view of the data flow through the data acquisition and online system. Taken from [94].

The software trigger (described in [95]) operates by determining the number of PMT hits within a 200ns sliding window, N_{200} , coincides with the maximum time that a Cherenkov photon would take to traverse the length of the SK tank [92]. For lower energy events that generate fewer photons, this technique is useful for eliminating background processes like dark noise and radioactive decay which would be expected to separate in time. When the value of N_{200} exceeds some threshold, a software trigger is issued. There are several trigger thresholds used within the SK-IV period which are detailed in Table 2.2. If one of these thresholds is met, the PMT hits within an extended

time window are also read out and saved to disk. In the special case of an event that exceeds the SHE trigger but does not exceed the OD trigger, the AFT trigger looks for delayed coincidences of 2.2MeV gamma rays emitted from neutron capture in a $535\mu\text{s}$ window after the SHE trigger. A similar but more complex “Wideband Intelligent Trigger (WIT)” has been deployed and is described in [90].

Trigger	Acronym	Condition	Extended time window (μs)
Super Low Energy	SLE	>34/31 hits	1.3
Low Energy	LE	>47 hits	40
High Energy	HE	>50 hits	40
Super High Energy	SHE	>70/58 hits	40
Outer Detector	OD	>22 hits in OD	N/A

Table 2.2: The trigger thresholds and extended time windows saved around an event which were utilised throughout the SK-IV period. The exact thresholds can change and the values listed here represent the thresholds at the start and end of the SK-IV period.

2.1.4 Cherenkov Radiation

Cherenkov light is emitted from any highly energetic charged particle traveling with relativistic velocity, β , greater than the local speed of light in a medium [96]. Cherenkov light is formed at the surface of a cone with characteristic pitch angle,

$$\cos(\theta) = \frac{1}{\beta n}. \quad (2.2)$$

where n is the refractive index of the medium. Consequently, the Cherenkov momentum threshold, P_{thres} , is dependent upon the mass, m , of the charged particle moving through the media,

$$P_{thres} = \frac{m}{\sqrt{n^2 - 1}} \quad (2.3)$$

639 For water, where $n = 1.33$, the Cherenkov threshold momentum and energy for
 640 various particles are given in Table 2.3. In contrast, γ -rays are detected indirectly via
 641 the combination of photons generated by Compton scattering and pair production.
 642 The threshold for detection in the SK detector is typically higher than the threshold
 643 for photon production. This is due to the fact that the attenuation of photons in the
 644 water means that typically $\sim 75\%$ of Cherenkov photons reach the ID PMTs. Then the
 645 collection and quantum efficiencies described in subsection 2.1.1 result in the number
 646 of detected photons being lower than the number of photons which reach the PMTs.

Particle	Threshold Momentum (MeV)	Threshold Energy (MeV)
Electron	0.5828	0.7751
Muon	120.5	160.3
Pion	159.2	211.7
Proton	1070.0	1423.1

Table 2.3: The threshold momentum and energy for a particle to generate Cherenkov light in ultrapure water, as calculated in Equation 2.2 in ultrapure water which has refractive index $n = 1.33$.

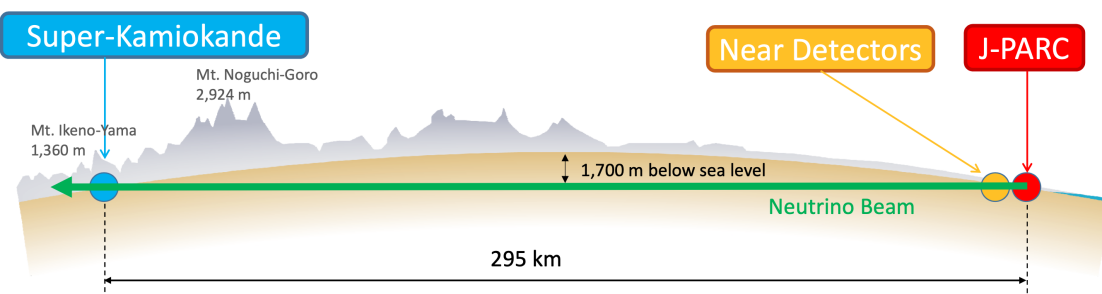
647 The Frank-Tamm equation [97] describes the relationship between the number of
 648 Cherenkov photons generated per unit length, dN/dx , the wavelength of the photons
 649 generated, λ , and the relativistic velocity of the charged particle,

$$\frac{d^2N}{dxd\lambda} = 2\pi\alpha \left(1 - \frac{1}{n^2\beta^2}\right) \frac{1}{\lambda^2}. \quad (2.4)$$

650 where α is the fine structure constant. For a 100MeV momentum electron, approx-
 651 imately 330 photons will be produced per centimeter in the $300\text{nm} \leq \lambda \leq 700\text{nm}$
 652 region which the ID PMTs are most sensitive to [80].

653 2.2 The Tokai to Kamioka Experiment

654 The Tokai to Kamioka (T2K) experiment is a long-baseline neutrino oscillation experi-
 655 ment located in Japan. Proposed in the early 2000s [98,99] to replace K2K [100], T2K
 656 was designed to observe electron neutrino appearance whilst precisely measuring
 657 the oscillation parameters associated with muon neutrino disappearance [101]. The
 658 experiment consists of a neutrino beam generated at the Japan Proton Accelerator
 659 Research Complex (J-PARC), a suite of near detectors situated 280m from the beam
 660 target, and the Super Kamiokande far detector positioned at a 295km baseline. The
 661 cross-section view of the T2K experiment is drawn in Figure 2.4.



662 **Figure 2.4:** The cross-section view of the Tokai to Kamioka experiment illustrating the beam
 663 generation facility at J-PARC, the near detector situated at a baseline of 280m and
 664 the Super Kamiokande far detector situated 295km from the beam target.

665 The T2K collaboration makes world-leading measurements of the $\sin^2(\theta_{23})$, Δm_{23}^2 ,
 666 and δ_{CP} oscillation parameters. Improvements in the precision and accuracy of pa-
 667 rameter estimates are still being made by including new data samples and developing
 668 the models which describe the neutrino interactions and detector responses [DB: Link](#)
 669 to Christophe's slides from Nu2022. Electron neutrino appearance was first observed

⁶⁶⁷ at T2K in 2014 [102] which accompanied a 7.3σ significance of a non-zero $\sin^2(\theta_{13})$
⁶⁶⁸ measurement.

⁶⁶⁹ The near detectors provide constraints on the beam flux and cross-section model
⁶⁷⁰ parameters used within the fit by observing the unoscillated neutrino beam. There
⁶⁷¹ are a host of detectors situated in the near detector hall (As illustrated in Figure 2.5);
⁶⁷² ND280 (subsection 2.2.2), INGRID (subsection 2.2.3), NINJA [103], WAGASCI [104],
⁶⁷³ and Baby-MIND [105]. The latter three are not currently used within the oscillation
⁶⁷⁴ analysis presented within this thesis.

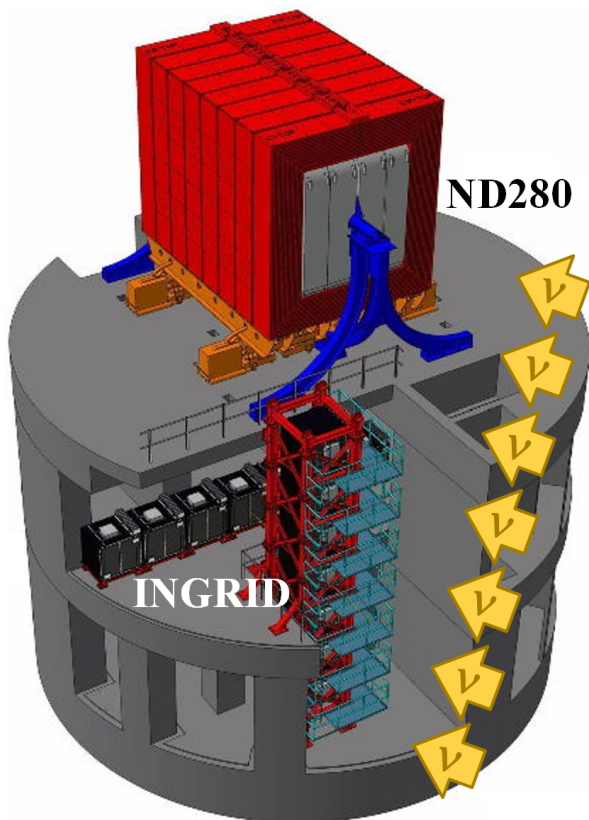


Figure 2.5: The near detector suite for the T2K experiment showing the ND280 and INGRID detectors. The distance between the detectors and the beam target is 280m.

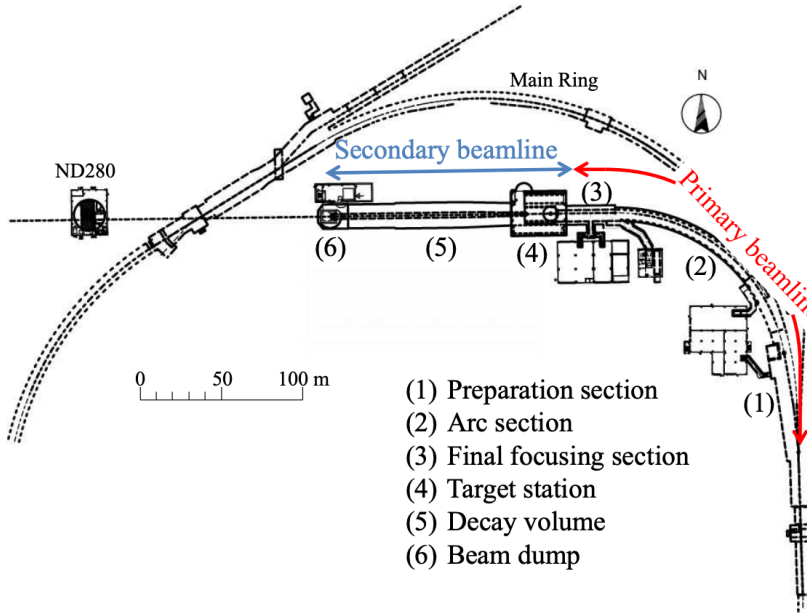
⁶⁷⁵ Whilst this thesis presents the ND280 in terms of its purpose for the oscillation
⁶⁷⁶ analysis, the detector can also make many cross-section measurements at neutrino
⁶⁷⁷ energies of $O(1)\text{GeV}$ for the different targets within the detector [106, 107]. These

678 measurements are of equal importance as they can lead the way in determining the
679 model parameters used in the interaction models for the future high-precision era of
680 neutrino physics.

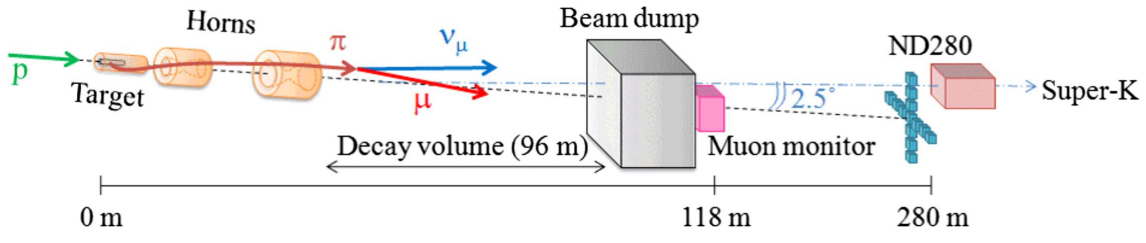
681 2.2.1 The Neutrino Beam

682 The neutrino beam used within the T2K experiment is described in [57, 108] and
683 summarised below. The accelerating facility at J-PARC is composed of two sections; the
684 primary and secondary beamlines. Figure 2.6 illustrates a schematic of the beamline,
685 focusing mostly on the components of the secondary beamline. The primary beamline
686 has three accelerators that progressively accelerate protons; a linear accelerator, a rapid-
687 cycling synchrotron, and the main-ring (MR) synchrotron. Once fully accelerated by
688 the MR, the protons have a kinetic energy of 30GeV. Eight bunches of these protons,
689 separated by 500ns, are extracted per “spill” from the MR and directed towards a
690 graphite target (A rod of length 91.4cm and diameter 2.6cm). Spills are extracted at
691 0.5Hz with $\sim 3 \times 10^{14}$ protons contained per spill.

692 The secondary beamline consists of three main components; the target station, the
693 decay volume, and the beam dump. The target station is comprised of the target, beam
694 monitors, and three magnetic focusing horns. The proton beam interacts with the
695 graphite target to form a secondary beam of mostly pions and kaons. The secondary
696 beam travels through a 96m long decay volume, generating neutrinos through the
697 following decays [57],



(a) Primary and secondary beamline



(b) Secondary beamline

Figure 2.6: Top panel: Bird's eye view of the most relevant part of primary and secondary beamline used within the T2K experiment. The primary beamline is the main-ring proton synchrotron, kicker magnet, and graphite target. The secondary beamline consists of the three focusing horns, decay volume, and beam dump. Figure taken from [108]. Bottom panel: The side-view of the secondary beamline including the focusing horns, beam dump and neutrino detectors. Figure taken from [109].

$$\pi^+ \rightarrow \mu^+ + \nu_\mu$$

$$\pi^- \rightarrow \mu^- + \bar{\nu}_\mu$$

$$K^+ \rightarrow \mu^+ + \nu_\mu$$

$$K^- \rightarrow \mu^- + \bar{\nu}_\mu$$

$$\rightarrow \pi^0 + e^+ + \nu_e$$

$$\rightarrow \pi^0 + e^- + \bar{\nu}_e$$

$$\rightarrow \pi^0 + \mu^+ + \nu_\mu$$

$$\rightarrow \pi^0 + \mu^- + \bar{\nu}_\mu$$

$$K_L^0 \rightarrow \pi^- + e^+ + \nu_e$$

$$K_L^0 \rightarrow \pi^+ + e^- + \bar{\nu}_e$$

$$\rightarrow \pi^- + \mu^+ + \nu_\mu$$

$$\rightarrow \pi^+ + \mu^- + \bar{\nu}_\mu$$

$$\mu^+ \rightarrow e^+ + \bar{\nu}_\mu + \nu_e$$

$$\mu^- \rightarrow e^- + \nu_\mu + \bar{\nu}_e$$

699 The electrically charged component of the secondary beam is focused towards the
 700 far detector by the three magnetic horns. These horns direct charged particles of a
 701 particular polarity towards SK whilst defocusing the oppositely charged particles.
 702 This allows a mostly neutrino or mostly antineutrino beam to be used within the
 703 experiment, denoted as “forward horn current (FHC)” or “reverse horn current (RHC)”
 704 respectively.

705 Figure 2.7 illustrates the different contributions to the FHC and RHC neutrino flux.

706 The low energy flux is dominated by the decay of pions whereas kaon decay becomes
 707 the dominant source of neutrinos for $E_\nu > 3\text{GeV}$. The “wrong-sign” component, which
 708 is the $\bar{\nu}_\mu$ background in a ν_μ beam, and the intrinsic irreducible ν_e background are
 709 predominantly due to muon decay for $E_\nu < 2\text{GeV}$. As the antineutrino cross-section is
 710 smaller than the neutrino cross-section, the wrong-sign component is more dominant
 711 in the RHC beam as compared to that in the FHC beam.

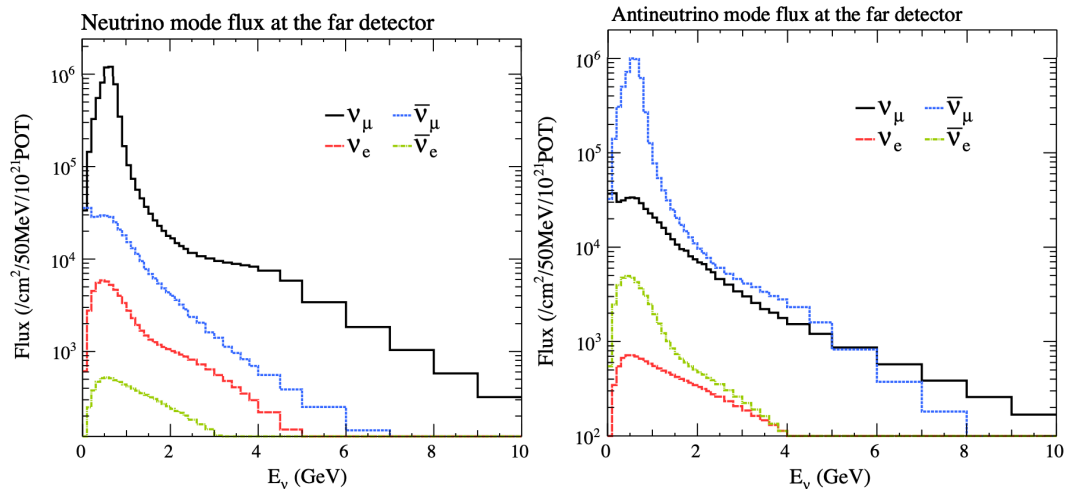


Figure 2.7: The Monte Carlo prediction of the energy spectrum for each flavour of neutrino (ν_e , $\bar{\nu}_e$, ν_μ and $\bar{\nu}_\mu$) in the neutrino dominated beam FHC mode (Left) and antineutrino dominated beam RHC mode (Right) expected at SK. Taken from [110].

712 The beam dump, situated at the end of the decay volume, stops all charged particles
 713 other than highly energetic muons ($p_\mu > 5\text{GeV}$). The MuMon detector monitors the

⁷¹⁴ penetrating muons to determine the beam direction and intensity which is used to
⁷¹⁵ constrain some of the beam flux systematics within the analysis [109, 111].

⁷¹⁶ The T2K experiment uses an off-axis beam to narrow the neutrino energy distribution.
⁷¹⁷ This was the first implementation of this technique in a long-baseline neutrino
⁷¹⁸ oscillation experiment after its original proposal [112]. Pion decay, $\pi \rightarrow \mu + \nu_\mu$, is a
⁷¹⁹ two-body decay. Consequently, the neutrino energy, E_ν , can be determined based on
⁷²⁰ the pion energy, E_π , and the angle at which the neutrino is emitted, θ ,

$$E_\nu = \frac{m_\pi^2 - m_\mu^2}{2(E_\pi - p_\pi \cos(\theta))}, \quad (2.5)$$

⁷²¹ where m_π and m_μ are the mass of the pion and muon respectively. For a fixed
⁷²² energy pion, the neutrino energy distribution is dependent upon the angle at which
⁷²³ the neutrinos are observed from the initial pion beam direction. For the 295km
⁷²⁴ baseline at T2K, $E_\nu = 0.6\text{GeV}$ maximises the electron neutrino appearance probability,
⁷²⁵ $P(\nu_\mu \rightarrow \nu_e)$, whilst minimising the muon disappearance probability, $P(\nu_\mu \rightarrow \nu_\mu)$.
⁷²⁶ Figure 2.8 illustrates the neutrino energy distribution for a range of off-axis angles, as
⁷²⁷ well as the oscillation probabilities most relevant to T2K.

⁷²⁸ 2.2.2 The Near Detector at 280m

⁷²⁹ Whilst all the near detectors are situated in the same “pit” located at 280m from the
⁷³⁰ beamline, the “ND280” detector is the off-axis detector which is situated at the same
⁷³¹ off-axis angle as the Super-Kamiokande far detector. It has two primary functions;
⁷³² firstly it measures the neutrino flux and secondly it counts the event rates of different
⁷³³ types of neutrino interactions. Both of these constrain the flux and cross-section

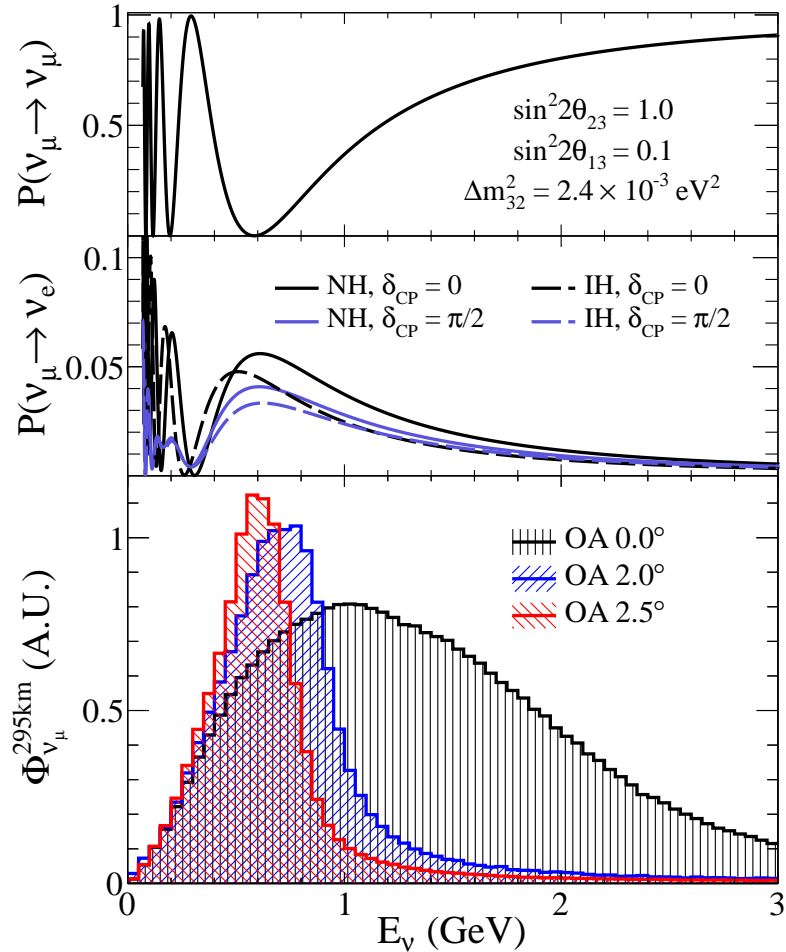


Figure 2.8: Top panel: T2K muon neutrino disappearance probability as a function of neutrino energy. Middle panel: T2K electron neutrino appearance probability as a function of neutrino energy. Bottom panel: The neutrino flux distribution for three different off-axis angles (Arbitrary units) as a function of neutrino energy.

734 systematics invoked within the model for a more accurate prediction of the expected
 735 event rate at the far detector.

736 As illustrated in Figure 2.9, the ND280 detector consists of several sub-detectors.
 737 The most important part of the detector for this analysis is the tracker region. This is
 738 comprised of two time projection chambers (TPCs) sandwiched between three fine
 739 grain detectors (FGDs). The FGDs contain both hydrocarbon plastics and water tar-
 740 gets for neutrino interactions and provide track reconstruction near the interaction
 741 vertex. The emitted charged particles can then propagate into the TPCs which pro-
 742 vide particle identification and momentum reconstruction. The FGDs and TPCs are

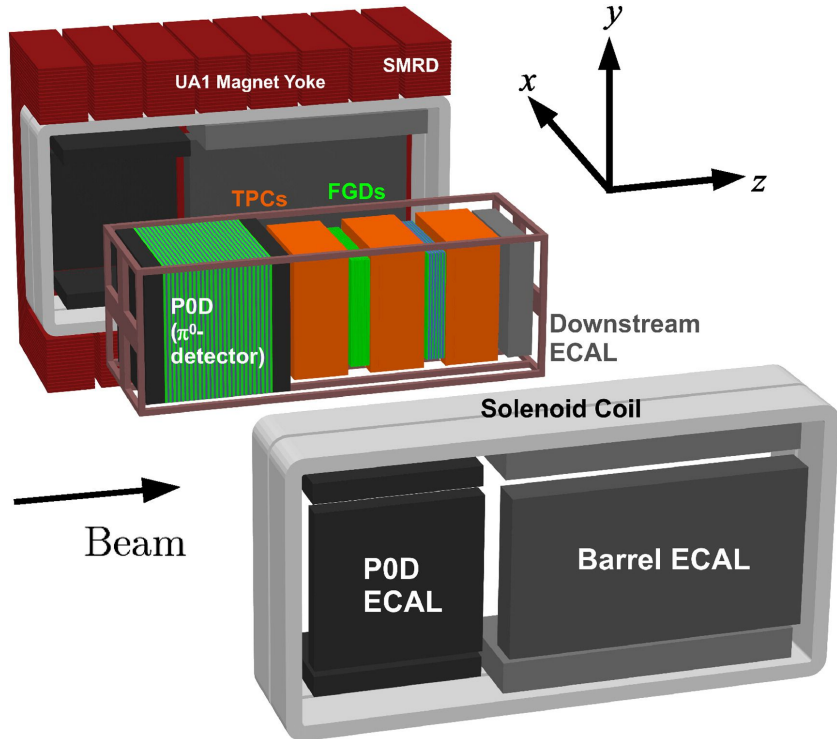


Figure 2.9: The components of the ND280 detector. The neutrino beam travels from left to right. Taken from [108].

743 further described in subsubsection 2.2.2.1 and subsubsection 2.2.2.2 respectively. The
 744 electromagnetic calorimeter (ECAL) encapsulates the tracker region alongside the π^0
 745 detector (P0D). The ECAL measures the deposited energy from photons emitted from
 746 interactions within the FGD. The P0D constrains the cross-section of neutral current
 747 interactions which generate neutral pions, which is one of the largest backgrounds in
 748 the electron neutrino appearance oscillation channel. The P0D and ECAL detectors
 749 are detailed in subsubsection 2.2.2.3 and subsubsection 2.2.2.4 respectively. The entire
 750 detector is located within a large yolk magnet which produces a 0.2T magnetic field.
 751 This design of the magnet also includes a scintillating detector called the side muon
 752 range detector (SMRD) which is used to track high-angle muons as well as acting as a
 753 cosmic veto. The SMRD is described in subsubsection 2.2.2.5.

754 2.2.2.1 Fine Grained Detectors

755 The T2K tracker region is comprised of two fine grained detectors (FGD) and three
756 Time Projection Chambers (TPC). A detailed description of the FGD design, construc-
757 tion, and assembly is found in [113] and summarised below. The FGDs are the primary
758 target for neutrino interactions with a mass of 1.1 tonnes per FGD. Alongside this,
759 the FGDs are designed to be able to track short-range particles which do not exit the
760 FGD. Typically, short-range particles are low momentum and are observed as tracks
761 that deposit a large amount of energy per unit length. This means the FGD needs
762 good granularity to resolve these particles. The FGDs have the best timing resolution
763 ($\sim 3\text{ns}$) of any of the sub-detectors of the ND280 detector. As such, the FGDs are
764 used for time of flight measurements to determine forward going positively charged
765 particles from backward going negatively charged particles. Finally, any tracks which
766 pass through multiple sub-detectors are required to be track matched to the FGD.

767 Both FDGs are made from square scintillator planes of side length 186cm and width
768 2.02cm. Each plane consists of two layers of 192 scintillator bars in an XY orientation.
769 A wave-length shift fiber is threaded through the center of each bar and is read out by
770 a multi-photon pixel counter (MPPC). FGD1 is the most upstream of the two FGDs
771 and contains 15 planes of carbon plastic scintillator which is a common target in
772 external neutrino scattering data. As the far detector is a pure water target, 7 of the 15
773 scintillator planes in FGD2 have been replaced with a hybrid water-scintillator target.
774 Due to the complexity of the nucleus, nuclear effects can not be extrapolated between
775 different nuclei. Therefore having the ability to take data on one target which is the
776 same as external data and another target which is the same as the far detector target is
777 beneficial for reliable model parameter estimates.

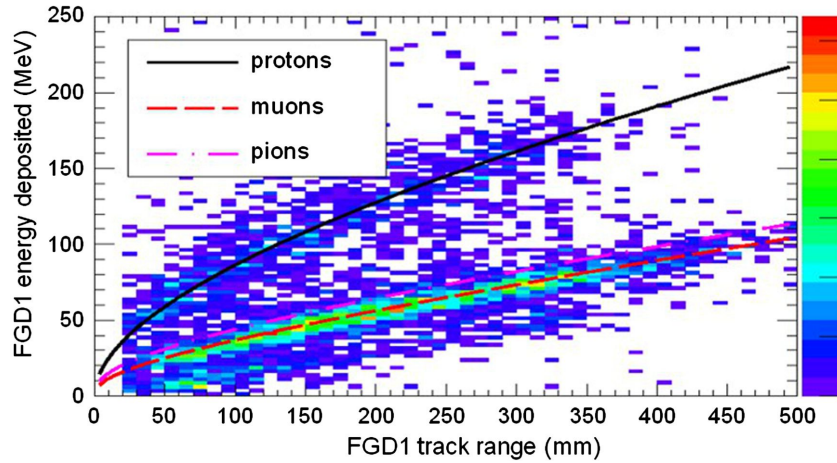


Figure 2.10: Comparison of data to Monte Carlo prediction of integrated deposited energy as a function of track length for particles that stopped in FGD1. Taken from [113].

The integrated deposited energy is used for particle identification. The FGD can distinguish protons from other charged particles by comparing the integrated deposited energy from data to Monte Carlo prediction as seen in Figure 2.10.

2.2.2.2 Time Projection Chambers

The majority of particle identification and momentum measurements within ND280 are provided by three Time Projection Chambers (TPCs) [114]. The TPCs are located on either side of the FGDs. They are located inside of the magnetic field meaning the momentum of a charged particle can be determined from the bending of the track.

Each TPC module consists of two gas-tight boxes, as shown in Figure 2.11, which are made of non-magnetic material. The outer box is filled with CO₂ which acts as an electrical insulator between the inner box and the ground. The inner box forms the field cage which produces a uniform electric drift field of $\sim 275\text{V/cm}$ and an argon gas mixture. Charged particles moving through this gas mixture ionize the gas mixture. The ionised charge is drifted towards micromega detectors which measure the ionization charge. The time and position information in the readout allows a three-dimensional image of the neutrino interaction.

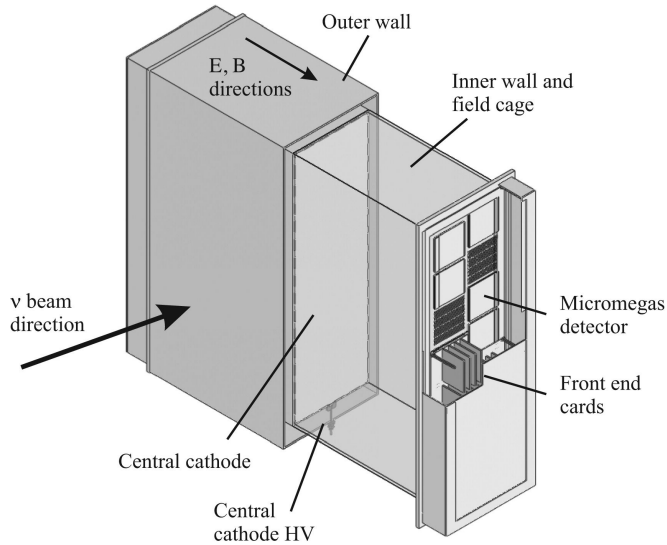


Figure 2.11: Schematic design of a Time Projection Chamber detector. Taken from [114].

The particle identification of tracks that pass through the TPCs is performed using

dE/dx measurements. Figure 2.12 illustrates the data to Monte Carlo distributions

of the energy lost by a charged particle passing through the TPC as a function of the

reconstructed particle momentum. The resolution is $7.8 \pm 0.2\%$ meaning that electrons

and muons can be distinguished. This allows reliable measurements of the intrinsic ν_e

component of the beam.

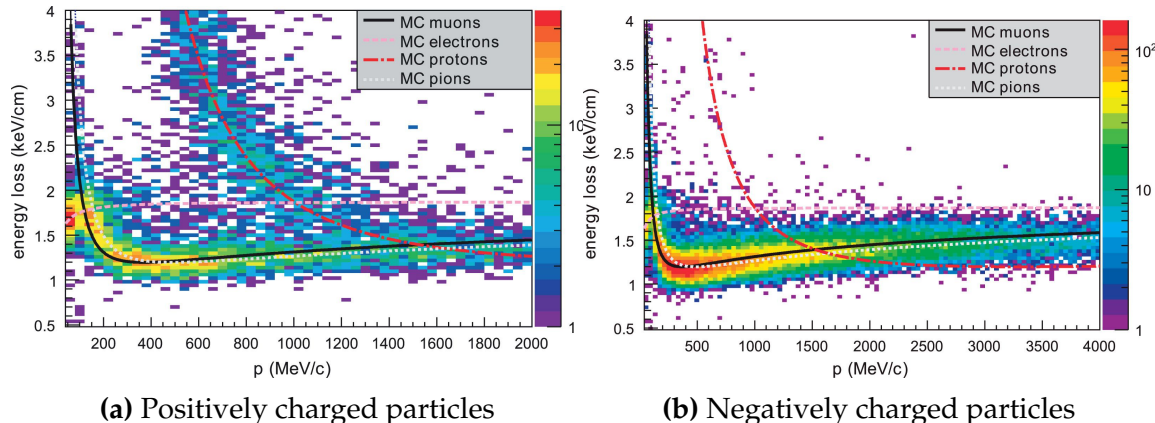


Figure 2.12: The distribution of energy loss as a function of reconstructed momentum for charged particles passing through the TPC, comparing data to Monte Carlo prediction. Taken from [114].

⁸⁰⁰ 2.2.2.3 π^0 Detector

⁸⁰¹ If one of the γ -rays from a $\pi^0 \rightarrow 2\gamma$ decay is missed at the far detector, the reconstruc-
⁸⁰² tion will determine that event to be electron-like. This is one of the main backgrounds
⁸⁰³ hindering the electron neutrino appearance searches. Therefore, the π^0 detector (P0D)
⁸⁰⁴ measures the cross-section of the neutral current induced neutral pion production on
⁸⁰⁵ a water target.

⁸⁰⁶ The P0D is a cube of approximately 2.5m length. The P0D consists of layers of
⁸⁰⁷ scintillating bars, brass and lead sheets, and water bags as illustrated in Figure 2.13.
⁸⁰⁸ Two electromagnetic calorimeters are positioned at the most upstream and most
⁸⁰⁹ downstream position in the sub-detector and the water target is situated in between
⁸¹⁰ them. The scintillator layers are built from two triangular bars orientated in opposite
⁸¹¹ directions to form a rectangular layer. Each triangular scintillator bar is threaded with
⁸¹² optical fiber which is read out by MPPCs. The high-Z brass and lead regions produce
⁸¹³ electron showers from the photons emitted in π^0 decay.

⁸¹⁴ The sub-detector can generate measurements of NC1 π^0 cross-sections on a water
⁸¹⁵ target by measuring the event rate both with and without the water target, with the
⁸¹⁶ cross-section on a water target being determined as the difference. The total active
⁸¹⁷ mass is 16.1 tonnes when filled with water and 13.3 tonnes when empty.

⁸¹⁸ 2.2.2.4 Electromagnetic Calorimeter

⁸¹⁹ The electromagnetic calorimeter [116] (ECal) encapsulates the P0D and tracking sub-
⁸²⁰ detectors. Its primary purpose is to aid π^0 reconstruction from any interaction in
⁸²¹ the tracker. To do this, it measures the energy and direction of photon showers from
⁸²² $\pi^0 \rightarrow 2\gamma$ decay. It can also distinguish pion and muon tracks depending on the shape
⁸²³ of the photon shower deposited.

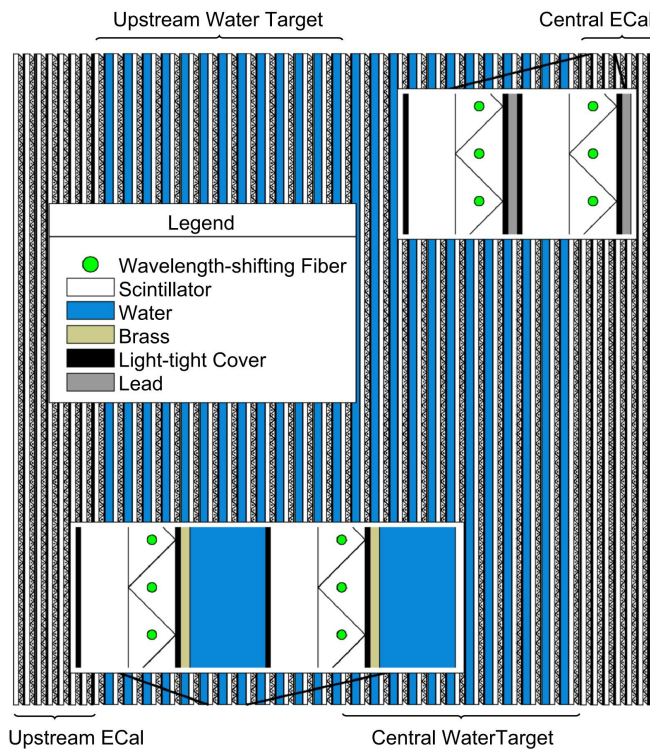


Figure 2.13: A schematic of the P0D side-view. Taken from [115].

The ECal is comprised of three sections; the P0D ECal which surrounds the P0D, the barrel ECal which encompasses the tracking region, and the downstream ECal which is situated downstream of the tracker region. The barrel and downstream ECals are tracking calorimeters that focus on electromagnetic showers from high-angle particles emitted from the tracking sub-detectors. Particularly in the TPC, high-angle tracks (those which travel perpendicularly to the beam-axis) can travel along a single scintillator bar resulting in very few hits. The width of the barrel and downstream ECal corresponds to ~ 11 electron radiation lengths to ensure $\sim 50\%$ of the energy of the π^0 is contained. As the P0D has its own calorimetry which reconstructs showers, the P0D ECal determines the energy which escapes the P0D.

Each ECal is constructed of multiple layers of scintillating bars sandwiched between lead sheets. The scintillating bars are threaded with optical fiber and read out by MPPCs. Each sequential layer of the scintillator is orientated perpendicular to the previous which allows a two-dimensional readout, which when temporal, information

⁸³⁸ is included results in three-dimension event displays. The target mass of the P0D ECal,
⁸³⁹ barrel ECal, and downstream ECal are 1.50, 4.80 and 6.62 tonnes respectively.

⁸⁴⁰ **2.2.2.5 Side Muon Range Detector**

⁸⁴¹ As illustrated in Figure 2.9, the ECal, FGDs, P0D, and TPCs are enclosed within the
⁸⁴² UA1 magnet. Originally designed for the NOMAD [117] experiment and reconditioned
⁸⁴³ for use in the T2K experiment [118], the UA1 magnet provides a uniform horizontal
⁸⁴⁴ magnetic field of $0.2 \pm 2 \times 10^{-4}$ T.

⁸⁴⁵ Built into the UA1 magnet, the side muon range detector (SMRD) [119] monitors
⁸⁴⁶ high-energy muons which leave the tracking region and permeate through the ECal.
⁸⁴⁷ It additionally acts as a cosmic muon veto and trigger.

⁸⁴⁸ **2.2.3 The Interactive Neutrino GRID**

⁸⁴⁹ The Interactive Neutrino GRID (INGRID) detector is situated within the same “pit” as
⁸⁵⁰ the other near detectors. It is aligned with the beam in the “on-axis” position and mea-
⁸⁵¹ sures the beam direction, spread, and intensity. The detector was originally designed
⁸⁵² with 16 identical modules [108] (two modules have since been decommissioned) and a
⁸⁵³ “proton” module. The design of the detector is cross-shaped with length and height
⁸⁵⁴ 10m × 10m as illustrated in Figure 2.14.

⁸⁵⁵ Each module is composed of iron sheets interlaced with eleven tracking scintillator
⁸⁵⁶ planes for a total target mass of 7.1 tonnes per module. The scintillator design is an X-Y
⁸⁵⁷ pattern of 24 bars in both orientations, where each bar contains wave-length shifting
⁸⁵⁸ fibers which are connected to multi-pixel photon counters (MPPCs). The MPPCs
⁸⁵⁹ convert detected photons into electrical signals via photodiodes. This is then read
⁸⁶⁰ out by Trip-T front-end electronics [120] and passed to the readout merging modules

⁸⁶¹ along with timing information from the clock module. Each module is encapsulated
⁸⁶² inside veto planes to aid the rejection of charged particles entering the module.

⁸⁶³ The proton module is different from the other modules in that it consists of entirely
⁸⁶⁴ scintillator planes with no iron target. The scintillator bars are also smaller than those
⁸⁶⁵ used in the other modules to increase the granularity of the detector and improve
⁸⁶⁶ tracking capabilities. The module sits in the center of the beamline and is designed to
⁸⁶⁷ give precise measurements of quasi-elastic charged current interactions to evaluate
⁸⁶⁸ the performance of the Monte Carlo simulation of the beamline.

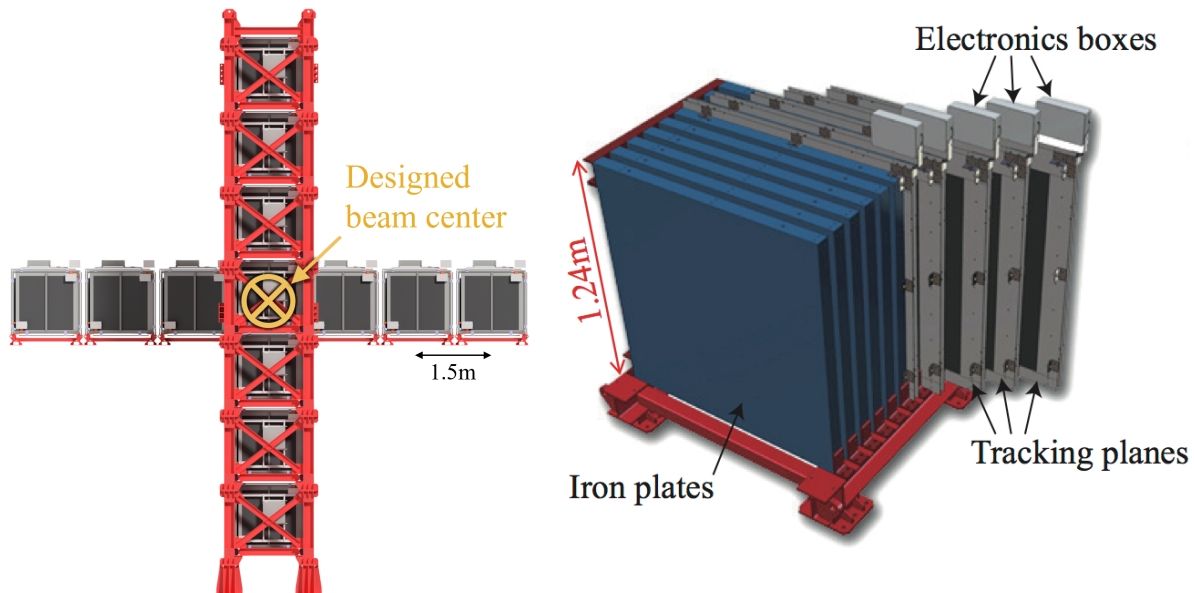


Figure 2.14: Left panel: The Interactive Neutrino GRID on-axis Detector. 14 modules are arranged in a cross-shape configuration, with the center modules being directly aligned with the on-axis beam. Right panel: The layout of a single module of the INGRID detector. Both figures are recreated from [108].

⁸⁶⁹ The INGRID detector can measure the beam direction to an uncertainty of 0.4mrad
⁸⁷⁰ and the beam center within a resolution of 10cm [108]. The beam direction in both the
⁸⁷¹ vertical and horizontal directions is discussed in [121] and it is found to be in good
⁸⁷² agreement with the MUMON monitor described in subsection 2.2.1.

873 **Chapter 3**

874 **Bayesian Statistics and Markov Chain
Monte Carlo Techniques**

876 The analysis throughout this thesis is based upon a Bayesian oscillation analysis. To
877 extract the oscillation parameters, a Markov Chain Monte Carlo (MCMC) method is
878 used. This chapter explains the theory of how parameter estimates can be determined
879 using this technique and condenses the material found in the literature [122–125].

880 The oscillation parameter determination presented within this thesis is built upon a
881 simultaneous fit to the near detector, far detector beam, and atmospheric neutrino data.
882 In total, there are four oscillation parameters of interest ($\sin^2(\theta_{23})$, $\sin^2(\theta_{13})$, Δm_{23}^2 ,
883 and δ_{CP}), two oscillation parameters to which this study will not be sensitive ($\sin^2(\theta_{12})$
884 , Δm_{12}^2) and many nuisance parameters that control the systematic uncertainty models
885 invoked within this study. The systematic uncertainties can be grouped into categories
886 depending on how they are defined; 574 bin-normalisations due to the near detector
887 response, 45 bin-normalisations to describe the far detector response to neutrino beam
888 events, 27 parameters to describe the detector response to atmospheric neutrino events,
889 100 to model the bin-normalisation due to beam flux uncertainties, 18 which model the
890 atmospheric flux uncertainties, and 87 to describe the correlated cross-section model.
891 An alternative parameterisation, where the far detector response is correlated between
892 the beam and atmospheric samples, replaces the bin-normalisation parameters with
893 224 shift and smear systematics. Section [DB: Link to Systematics Chapter](#) describes
894 the systematic model in more depth.

895 The MCMC technique generates a multi-dimensional probability distribution across
896 all of the model parameters used in the fit. To determine the parameter estimate of a
897 single parameter, this multi-dimensional object is integrated over all other parameters.
898 This process is called Marginalisation and is further described in subsection 3.3.1.
899 Monte Carlo techniques approximate the probability distribution of each parameter
900 within the limit of generating infinite samples. As ever, generating a large number of
901 samples is time and resource-dependent. Therefore, an MCMC technique is utilised
902 within this analysis to reduce the required number of steps to sufficiently sample the
903 parameter space. This technique is described in further detail in subsection 3.2.1.

904 3.1 Bayesian Statistics

905 According to Bayesian Inference, observables and parameters of a statistical model are
906 treated on an equal footing. To estimate model parameters $\vec{\theta}$ from some data D , one
907 needs to define the joint probability distribution $P(D|\vec{\theta})$ which can be described as the
908 prior distribution for model parameters $P(\vec{\theta})$ and the likelihood of the data given the
909 model parameters $P(D|\vec{\theta})$,

$$P(D, \vec{\theta}) = P(D|\vec{\theta})P(\vec{\theta}). \quad (3.1)$$

910 The prior distribution, $P(\vec{\theta})$, describes all previous knowledge about the parameters
911 within the model. For example, if the risk of developing health problems is known
912 to increase with age, the prior distribution would describe the increase. For the
913 purpose of this analysis, the prior distribution is typically the best-fit values taken
914 from external data measurements with a Gaussian uncertainty. The prior distribution

can also contain correlations between model parameters. In an analysis using Monte Carlo techniques, the likelihood of measuring some data assuming some set of model parameters is calculated by comparing the Monte Carlo prediction generated at that particular set of model parameters to the data.

It is parameter estimation that is important for this analysis and as such, we apply Bayes' theorem [126]. To calculate the probability for each parameter to have a certain value given the observed data $P(\vec{\theta}|D)$, known as the posterior distribution (often termed the posterior). This can be expressed as

$$P(\vec{\theta}|D) = \frac{P(D|\vec{\theta})P(\vec{\theta})}{\int P(D|\vec{\theta})P(\vec{\theta})d\vec{\theta}}. \quad (3.2)$$

The denominator in Equation 3.2 is the integral of the joint probability distribution over all values of all parameters used within the fit. For brevity, we say that the posterior distribution is

$$P(\vec{\theta}|D)\alpha P(D|\vec{\theta})P(\vec{\theta}). \quad (3.3)$$

In subsection 3.3.1, we see that for the cases used within this analysis, it is reasonable to know the posterior to some normalisation constant.

3.2 Monte Carlo Simulation

Monte Carlo techniques are used to numerically solve a complex problem that does not necessarily have an analytical solution. These techniques rely on building a large

931 ensemble of samples from an unknown distribution and then using the ensemble to
932 approximate the properties of the distribution.

933 An example that uses Monte Carlo techniques is to calculate the area underneath
934 a curve. For example, take the problem of calculating the area under a straight line
935 with gradient $M = 0.4$ and intercept $C = 1.0$. Analytically, one can calculate the area
936 under the line is equal to 30 units for $0 \leq x \leq 10$. Using Monte Carlo techniques,
937 one can calculate the area under this line by throwing many random values for the x
938 and y components of each sample and then calculating whether that point falls below
939 the line. The area can then be calculated by the ratio of points below the line to the
940 total number of samples thrown multiplied by the total area in which samples were
941 scattered. The study is shown in Figure 3.1 highlights this technique and finds the area
942 under the curve to be 29.9 compared to an analytical solution of 30.0. The deviation
943 of the numerical to analytical solution can be attributed to the number of samples
944 used in the study. The accuracy of the approximation in which the properties of the
945 Monte Carlo samples replicate those of the desired distribution is dependent on the
946 number of samples used. Replicating this study with a differing number of Monte
947 Carlo samples used in each study (As shown in Figure 3.2) highlights how the Monte
948 Carlo techniques are only accurate within the limit of a high number of samples.

949 Whilst the above example has an analytical solution, these techniques are just as
950 applicable to complex solutions. Clearly, any numerical solution is only as useful as its
951 efficiency. As discussed, the accuracy of the Monte Carlo technique is dependent upon
952 the number of samples generated to approximate the properties of the distribution.
953 Furthermore, if the positions at which the samples are evaluated are not 'cleverly'
954 picked, the efficiency of the Monte Carlo technique significantly drops. Given the
955 example in Figure 3.1, if the region in which the samples are scattered significantly
956 extends passed the region of interest, many calculations will be calculated but do

not add to the ability of the Monte Carlo technique to achieve the correct result. For instance, any sample evaluated at a $y \geq 5$ could be removed without affecting the final result. This does bring in an aspect of the ‘chicken and egg’ problem in that to achieve efficient sampling, one needs to know the distribution beforehand.

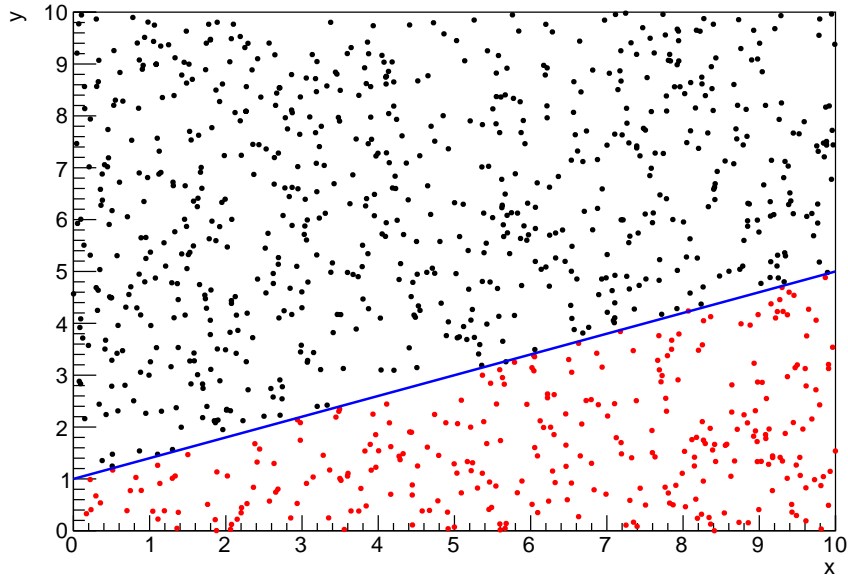


Figure 3.1: Example of using Monte Carlo techniques to find the area under the blue line. The gradient and intercept of the line are 0.4 and 1.0 respectively. The area found to be under the curve using one thousand samples is 29.9 units.

3.2.1 Markov Chain Monte Carlo

This analysis utilises a multi-dimensional probability distribution, with some dimensions being significantly more constrained than others. This could be from prior knowledge of parameter distributions from external data or un-physical regions in which parameters can not exist. Consequently, the Monte Carlo techniques used need to be as efficient as possible. For this analysis, the Markov Chain Monte Carlo (MCMC) technique is chosen. An MCMC technique is a Monte Carlo technique that uses a Markov chain to select which points at which to sample the parameter distribution.

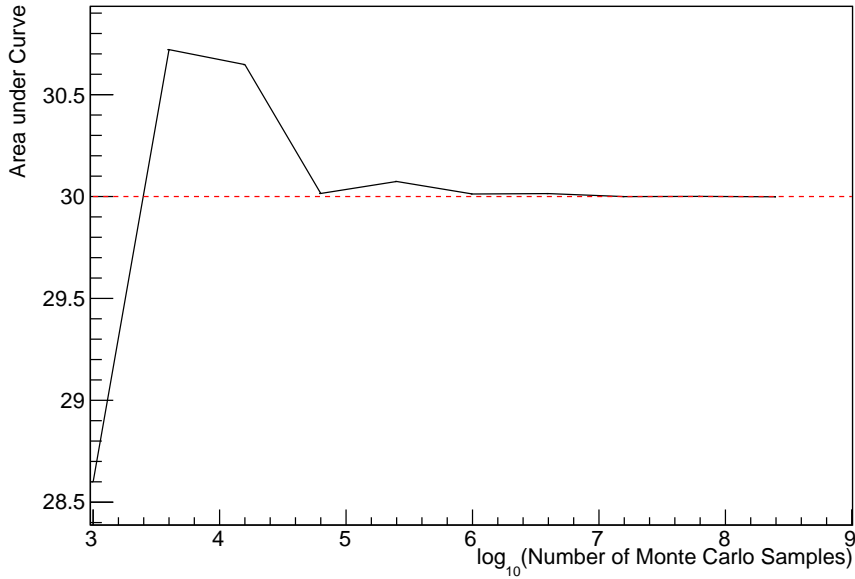


Figure 3.2: The area under a line of gradient 0.4 and intercept 1.0 for the range $0 \leq x \leq 10$ as calculated using Monte Carlo techniques as a function of the number of samples used in each repetition. The analytical solution to the area is 30 units as given by the red line.

969 This technique performs a semi-random stochastic walk through the allowable pa-
 970 rameter space. This builds a posterior distribution which has the property that the
 971 density of sampled points is proportional to the probability density of that parame-
 972 ter. This does mean that the samples produced by this technique are not statistically
 973 independent but they will cover the space of the distribution.

974 A Markov chain functions by selecting the position of step \vec{x}_{i+1} based on the
 975 position of \vec{x}_i . The space in which the Markov chain selects samples is dependent
 976 upon the total number of parameters utilised within the fit, where a discrete point in
 977 this space is described by the N-dimensional space \vec{x} . In a perfectly operating Markov
 978 chain, the position of the next step depends solely on the previous step and not on the
 979 further history of the chain (\vec{x}_0, \vec{x}_1 , etc.). However, in solving the multi-dimensionality
 980 of the fit used within this analysis, each step becomes correlated with several of
 981 the steps preceding itself. This behaviour is further explained in subsection 3.2.3.
 982 Providing the MCMC chain is well optimised, it will begin to converge towards a

unique stationary distribution. The period between the chain's initial starting point and the convergence to the unique stationary distribution is colloquially known as the burn-in period. This is discussed further in subsection 3.2.3. Once the chain reaches the stationary distribution, all points sampled after that point will look like samples from that distribution.

Further details of the theories underpinning MCMC techniques are discussed in [123] but can be summarised by the requirement that the chain satisfies the three 'regularity conditions':

- Irreducibility: From every position in the parameter space \vec{x} , there must exist a non-zero probability for every other position in the parameter space to be reached.
- Recurrence: Once the chain arrives at the stationary distribution, every step following from that position must be samples from the same stationary distribution.
- Aperiodicity: The chain must not repeat the same sequence of steps at any point throughout the sampling period.

The output of the chain after burn-in (ie. the sampled points after the chain has reached the stationary distribution) can be used to approximate the posterior distribution and model parameters $\vec{\theta}$. To achieve the requirement that the unique stationary distribution found by the chain be the posterior distribution, one can use the Metropolis-Hastings algorithm. This guides the stochastic process depending on the likelihood of the current proposed step compared to that of the previous step. Implementation and other details of this technique are discussed in subsection 3.2.2.

1004 3.2.2 Metropolis-Hastings Algorithm

1005 As a requirement for MCMCs, the Markov chain implemented in this technique must
 1006 have a unique stationary distribution that is equivalent to the posterior distribution.
 1007 To ensure this requirement and that the regularity conditions are met, this analysis
 1008 utilises the Metropolis-Hastings (MH) algorithm [127, 128]. For the i^{th} step in the chain,
 1009 the MH algorithm determines the position in the parameter space to which the chain
 1010 moves to based on the current step, \vec{x}_i , and the proposed step, \vec{y}_{i+1} . The proposed step
 1011 is randomly selected from some proposal function $f(\vec{x}_{i+1}|\vec{x}_i)$, which depends solely
 1012 on the current step (ie. not the further history of the chain). The next step in the chain
 1013 \vec{x}_{i+1} can be either the current step or the proposed step determined by whether the
 1014 proposed step is accepted or rejected. To decide if the proposed step is selected, the
 1015 acceptance probability, $\alpha(\vec{x}_i, \vec{y}_i)$, is calculated as

$$\alpha(\vec{x}_i, \vec{y}_{i+1}) = \min\left(1, \frac{P(\vec{y}_{i+1}|D)f(\vec{x}_i|\vec{y}_{i+1})}{P(\vec{x}_i|D)f(\vec{y}_{i+1}|\vec{x}_i)}\right). \quad (3.4)$$

1016 Where $P(\vec{y}_{i+1}|D)$ is the posterior distribution as introduced in section 3.1. To
 1017 simplify this calculation, the proposal function is required to be symmetric such that
 1018 $f(\vec{x}_i|\vec{y}_{i+1}) = f(\vec{y}_{i+1}|\vec{x}_i)$. In practice, a multi-variate Gaussian distribution is used to
 1019 throw parameter proposals from. This reduces Equation 3.4 to

$$\alpha(\vec{x}_i, \vec{y}_{i+1}) = \min\left(1, \frac{P(\vec{y}_{i+1}|D)}{P(\vec{x}_i|D)}\right). \quad (3.5)$$

1020 After calculating this quantity, a random number, β , is generated uniformly be-
 1021 tween 0 and 1. If $\beta \leq \alpha(\vec{x}_i, \vec{y}_{i+1})$, the proposed step is accepted. Otherwise, the chain
 1022 sets the next step equal to the current step and this procedure is repeated. This can be
 1023 interpreted as if the posterior probability of the proposed step is greater than that of
 1024 the current step, ($P(\vec{y}_{i+1}|D) \geq P(\vec{x}_i|D)$), the proposed step will always be accepted.
 1025 If the opposite is true, ($P(\vec{y}_{i+1}|D) \leq P(\vec{x}_i|D)$), the proposed step will be accepted
 1026 with probability $P(\vec{x}_i|D)/P(\vec{y}_{i+1}|D)$. This ensures that the Markov chain does not get
 1027 trapped in any local minima in the potentially non-Gaussian posterior distribution.
 1028 The outcome of this technique is that the density of steps taken in a discrete region is
 1029 directly proportional to the probability density in that region.

1030 3.2.3 MCMC Optimisation

1031 As discussed in subsection 3.2.2, the proposal function invoked within the MH algo-
 1032 rithm can take any form and the chain will still converge to the stationary distribution.
 1033 As discussed in [DB: Link to Analysis Strategy Section](#), this analysis performs the
 1034 Monte Carlo reweighting on an event-by-event basis. This requires significant com-
 1035 putational resources to perform a parameter fit. Therefore, the number of steps taken
 1036 before the unique stationary distribution is found should be minimised as only steps
 1037 after convergence add information to the fit. Furthermore, the chain should entirely
 1038 cover the allowable parameter space to ensure that all values have been considered.
 1039 Tuning the distance that the proposal function jumps between steps on a parameter-
 1040 by-parameter basis can both minimise the length of the burn-in period and ensure that
 1041 the correlation between step \vec{x}_i and \vec{x}_j is sufficiently small.

1042 The effect of changing the width of the proposal function is highlighted in Figure 3.3.
 1043 Three scenarios, each with the same underlying stationary distribution (A Gaussian of
 1044 width 1.0 and mean 0.), are presented. The only difference between the three scenarios

is the width of the proposal function, colloquially known as the ‘step size σ ’. Each scenario starts at an initial parameter value of 10.0 which would be considered an extreme variation. For the case where $\sigma = 0.1$, it is clear to see that the chain takes a long time to reach the expected region of the parameter. This indicates that this chain would have a large burn-in period and does not converge to the stationary distribution until step ~ 500 . Furthermore, whilst the chain does move towards the expected region, each step is significantly correlated with the previous. Considering the case where $\sigma = 5.0$, the chain approaches the expected parameter region almost instantly meaning that the burn-in period is not significant. However, there are clearly large regions of steps where the chain does not move. This is likely due to the chain proposing steps in the tails of the distribution which have a low probability of being accepted. Consequently, this chain would take a significant number of steps to fully span the allowable parameter region. For the final scenario, where $\sigma = 0.5$, you can see a relatively small burn-in period of approximately 100 steps. Once the chain reaches the stationary distribution, it moves throughout the expected region of parameter values many times, sufficiently sampling the full parameter region. This example is a single parameter varying across a continuous distribution and does not fully reflect the difficulties in the many-hundred multi-variate parameter distribution used within this analysis. However, it does give a conceptual idea of the importance of selecting the proposal function and associated step size.

As discussed, step size tuning directly correlates to the average step acceptance rate. If the step size is too small, many steps will be accepted but the chain moves slowly. If the opposite is true, many steps will be rejected as the chain proposes steps in the tails of the distribution. Discussion in [129] suggests that the ‘ideal’ acceptance rate of a high dimension MCMC chain should be approximately $\sim 25\%$. An “ideal” step size [129] of

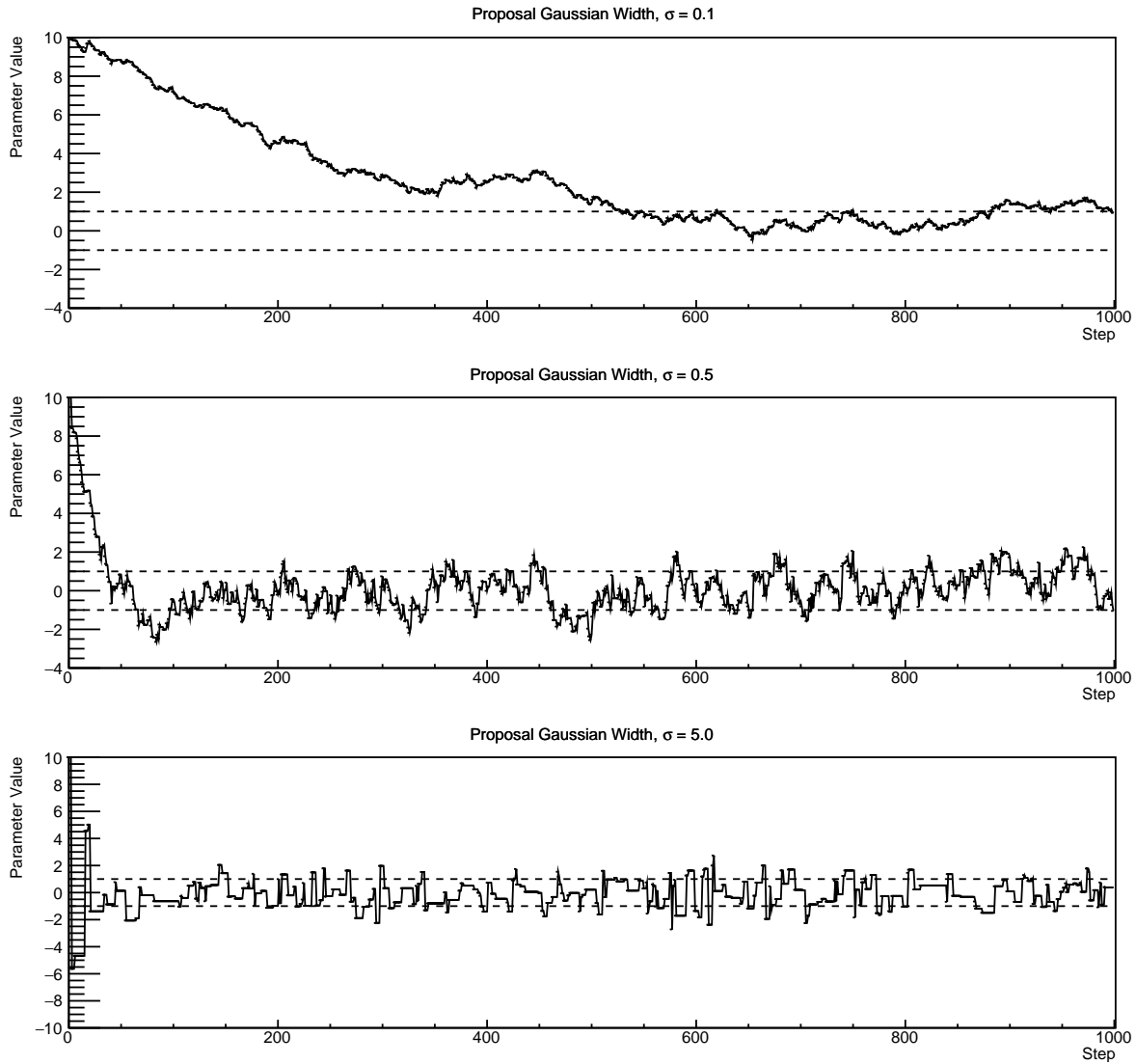


Figure 3.3: Three MCMC chains, each with a stationary distribution equal to a Gaussian centered at 0 and width 1 (As indicated by the black dotted lines). All of the chains use a Gaussian proposal function but have different widths (or ‘step size σ ’). The top panel has $\sigma = 0.1$, middle panel has $\sigma = 0.5$ and the bottom panel has $\sigma = 5.0$.

$$\sigma = \frac{2.4}{N_p}, \quad (3.6)$$

1071 where N_p is the number of parameters included in the MCMC fit. However, the
 1072 complex correlations between systematics mean that some parameters have to be hand

₁₀₇₃ tuned and many efforts have been taken to select a set of parameter-by-parameter step
₁₀₇₄ sizes to approximately reach the ideal acceptance rate.

₁₀₇₅ Figure 3.3 highlights the likelihood as calculated by the fit in [DB: Link to AsimovA](#)
₁₀₇₆ [Sensitivity Section](#) as a function of the number of steps in each chain. In practice,
₁₀₇₇ many independent MCMC chains are run simultaneously to parallelise the task of
₁₀₇₈ performing the fit. This figure overlays the distribution found in each chain. As seen,
₁₀₇₉ the likelihood decreases from its initial value and converges towards a stationary
₁₀₈₀ distribution after $\sim 1 \times 10^5$ steps. Each fit (whether it be different asimov fits or data
₁₀₈₁ fit) will have a different set of preferred parameter values which results in a different
₁₀₈₂ stationary distribution. For each fit presented in this thesis, a burn-in period of 1×10^5
₁₀₈₃ steps was found to be sufficient.

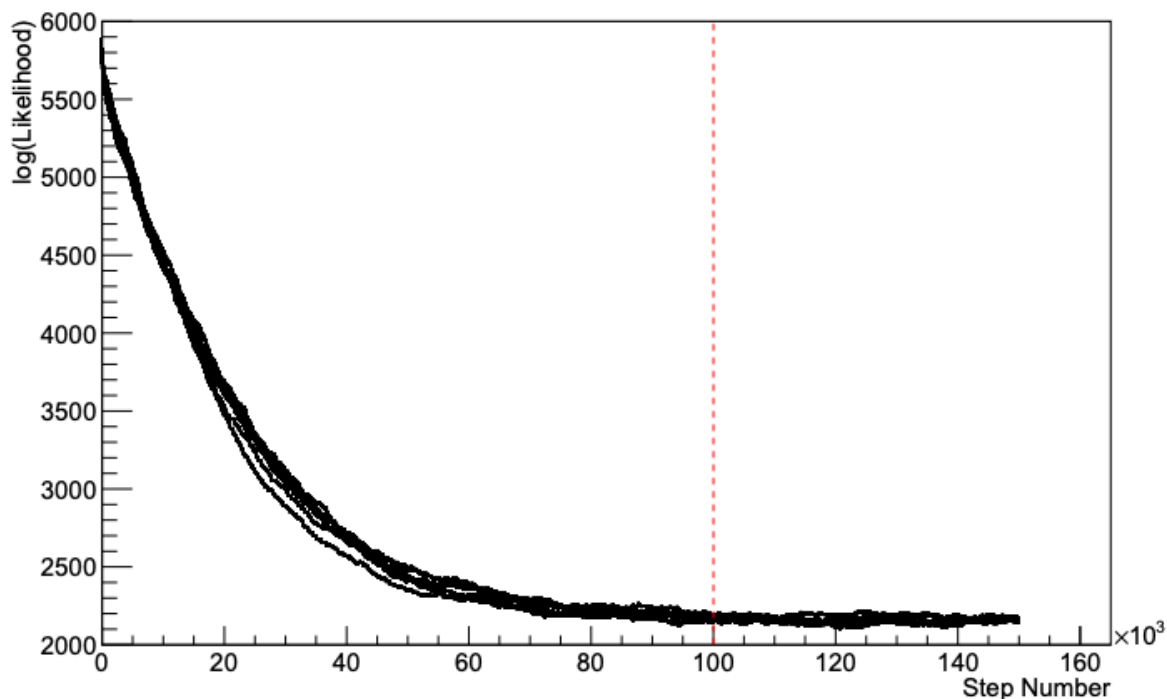


Figure 3.4: The log-likelihood from the fit detailed in [DB: Link to AsimovA](#) [Sensitivity Section](#) as a function of the number of steps accumulated in each fit. Many independent MCMC chains were run in parallel and overlaid on this plot. The red line indicates the 1×10^5 step burn-in period after which the log-likelihood becomes stable.

1084 3.3 Understanding the MCMC Results

1085 Whilst section 3.1 and section 3.2 describe how to interpret Bayesian statistics and
1086 explains the MCMC techniques used within this analysis, there is no mention of
1087 how to interpret the output of the chain. The posterior distribution output from the
1088 chain is a high dimension object, with as many dimensions as there are parameters
1089 included in the fit. However, this multi-dimensional object is difficult to conceptualize
1090 so parameter estimations are often presented in one or two-dimensional projections
1091 of this probability distribution. To do this, we invoke the marginalisation technique
1092 highlighted in subsection 3.3.1.

1093 3.3.1 Marginalisation

1094 The output of the MCMC chain is a highly dimensional probability distribution
1095 which is very difficult to interpret. From the standpoint of an oscillation analysis
1096 experiment, the one or two-dimensional ‘projections’ of the oscillation parameters of
1097 interest are most relevant. Despite this, the best fit values and uncertainties on the
1098 oscillation parameters of interest should correctly encapsulate the correlations to the
1099 other systematic uncertainties (colloquially called ‘nuisance’ parameters). For this joint
1100 beam and atmospheric analysis, the oscillation parameters of interest are $\sin^2(\theta_{23})$,
1101 $\sin^2(\theta_{13})$, Δm_{23}^2 , and δ_{CP} . All other parameters (Including the oscillation parameter
1102 this fit is insensitive to) are deemed nuisance parameters. To generate these projections,
1103 we rely upon integrating the posterior distribution over all nuisance parameters. This
1104 is called marginalisation. A simple example of this technique is to imagine the scenario
1105 where two coins are flipped. To determine the probability that the first coin returned
1106 a ‘head’, the exact result of the second coin flip is disregarded and simply integrated

1107 over. For the parameters of interest, $\vec{\theta}_i$, we can calculate the marginalised posterior by
1108 integrating over the nuisance parameters, $\vec{\theta}_n$. In this case, Equation 3.2 becomes

$$P(\vec{\theta}_i|D) = \frac{\int P(D|\vec{\theta}_i, \vec{\theta}_n)P(\vec{\theta}_i, \vec{\theta}_n)d\vec{\theta}_n}{\int P(D|\vec{\theta})P(\vec{\theta})d\vec{\theta}} \quad (3.7)$$

1109 Where $P(\vec{\theta}_i, \vec{\theta}_n)$ encodes the prior knowledge about the uncertainty and correlations
1110 between the parameters of interest and the nuisance parameters. In practice, this
1111 is simply taking the one or two-dimensional projection of the multi-dimensional
1112 probability distribution.

1113 Whilst in principle an easy solution to a complex problem, correlations between the
1114 interesting and nuisance parameters can bias the marginalised results. A similar effect
1115 is found when the parameters being marginalised over have non-Gaussian probability
1116 distributions. For example, Figure 3.5 highlights the marginalisation bias in the
1117 probability distribution found for a parameter when requiring a correlated parameter
1118 to have a positive parameter value. Due to the complex nature of this oscillation
1119 parameter fit presented in this thesis, there are certainly correlations occurring between
1120 the oscillation parameters of interest and the other nuisance parameters included in
1121 the fit.

1122 3.3.2 Parameter Estimation and Credible Intervals

1123 The purpose of this analysis is to determine the best fit values for the oscillation param-
1124 eters that the beam and atmospheric samples are sensitive to; $\sin^2(\theta_{23})$, $\sin^2(\theta_{13})$,
1125 Δm_{23}^2 , and δ_{CP} . Typically, the results presented take the form of one or two-dimension
1126 marginalised probability distributions for the appearance ($\sin^2(\theta_{13})$ and δ_{CP}) and

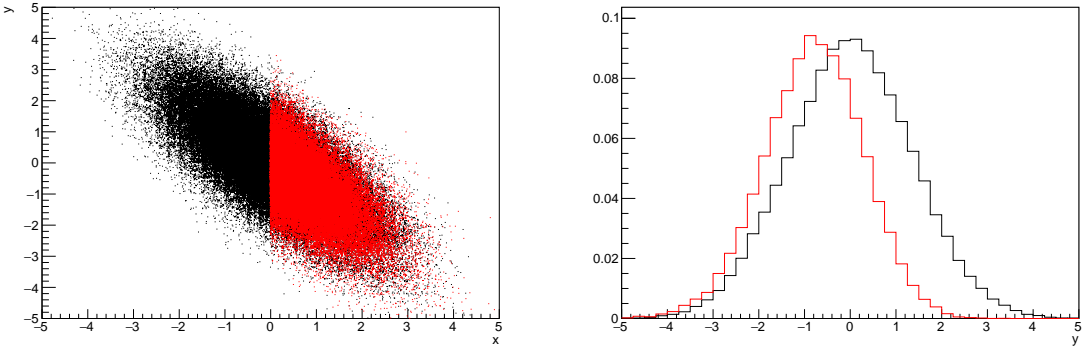


Figure 3.5: Left: The two dimensional probability distribution for two correlated parameters x and y . The red distribution shows the two dimensional probability distribution when $0 \leq x \leq 5$. Right: The marginalised probability distribution for the y parameter found when requiring the x to be bound between $-5 \leq x \leq 5$ and $0 \leq x \leq 5$ for the black and red distribution, respectively.

1127 disappearance ($\sin^2(\theta_{23})$ and Δm_{23}^2) parameters. The posterior probability density
 1128 taken from the output MCMC chain is binned in these parameters. The parameter
 1129 best-fit point is then taken to be the value that has the highest posterior probability.
 1130 This is performed in both one and two-dimensional projections.

1131 However, the single best-fit point in a given parameter is not of much use on its
 1132 own. We would also like to determine the uncertainty, or credible interval, on that
 1133 best-fit point. The definition of the 1σ credible interval is that we have 68% belief that
 1134 the parameter is within those bounds. For a more generalised definition, the credible
 1135 interval is the region of the posterior distribution that contains a specific fraction of
 1136 the total probability, such that

$$\int P(\theta|D)d\theta = \alpha \quad (3.8)$$

1137 Where θ is the parameter on which we calculate the credible interval. This technique
 1138 then calculates the $\alpha \times 100\%$ credible interval.

1139 In practice, this analysis uses the highest posterior density (HPD) credible intervals
 1140 which are calculated through the following method. First, the probability distribution
 1141 is area-normalised such that it has an integrated area equal to 1.0. The bins of proba-
 1142 bility are then summed from the highest to lowest until the sum exceeds the 1σ level
 1143 (0.68 in this example). This process is repeated for a range of credible intervals, notably
 1144 the 1σ , 2σ and 3σ along with other levels where the critical values for each level can
 1145 be found in [130]. This process can be repeated for the two-dimensional probability
 1146 distributions by creating two-dimensional contours of credible intervals rather than a
 1147 one-dimensional result.

1148 3.3.3 Application of Bayes' Theorem

1149 Due to the matter resonance, this analysis has some sensitivity to the mass hierarchy
 1150 of neutrino states (whether Δm_{23}^2 is positive or negative) and the octant of $\sin^2(\theta_{23})$
 1151 . The Bayesian approach utilised within this analysis gives an intuitive method of
 1152 model comparison by determining which hypothesis is most favourable. Taking the
 1153 ratio of Equation 3.3 for the two hypotheses of normal hierarchy, NH , and inverted
 1154 hierarchy, IH , gives

$$\frac{P(\vec{\theta}_{NH}|D)}{P(\vec{\theta}_{IH}|D)} = \frac{P(D|\vec{\theta}_{NH})}{P(D|\vec{\theta}_{IH})} \times \frac{P(\vec{\theta}_{NH})}{P(\vec{\theta}_{IH})}. \quad (3.9)$$

1155 The middle term defines the Bayes factor which is a data-driven interpretation of
 1156 how strong the data prefers one hierarchy to the other. For this analysis, equal priors
 1157 on both mass hierarchy hypotheses are chosen ($P(\vec{\theta}_{NH}) = P(\vec{\theta}_{IH}) = 0.5$). In practice,
 1158 the MCMC chain proposes a value of $|\Delta m_{23}^2|$ and then applies a 50% probability
 1159 that the value is sign flipped. Consequently, the Bayes factor can be calculated from

₁₁₆₀ the ratio of the probability density in either hypothesis. This equates to counting the
₁₁₆₁ number of steps taken in the normal and inverted hierarchies and taking the ratio. The
₁₁₆₂ same approach can be taken to compare the upper octant (UO) compared to the lower
₁₁₆₃ octant (LO) hypothesis of $\sin^2(\theta_{23})$.

₁₁₆₄ Whilst the value of the Bayes factor should always be shown, the Jeffreys scale [131]
₁₁₆₅ (highlighted in Table 3.1) gives an indication of the strength of preference for one model
₁₁₆₆ compared to the other. Other interpretations of the strength of preference of a model
₁₁₆₇ exist, e.g. the Kass and Raferty Scale [132].

$\log_{10}(B_{AB})$	B_{AB}	Strength of Preference
< 0.0	< 1	No preference for hypothesis A (Supports hypothesis B)
0.0 – 0.5	1.0 – 3.16	Preference for hypothesis A is weak
0.5 – 1.0	3.16 – 10.0	Preference for hypothesis A is substantial
1.0 – 1.5	10.0 – 31.6	Preference for hypothesis A is strong
1.5 – 2.0	31.6 – 100.0	Preference for hypothesis A is very strong
> 2.0	> 100.0	Decisive preference for hypothesis A

Table 3.1: Jeffreys scale for strength of preference for two models A and B as a function of the calculated Bayes factor ($B_{AB} = B(A/B)$) between the two models [131]. The original scale is given in terms of $\log_{10}(B(A/B))$ but converted to linear scale for easy comparison throughout this thesis.

₁₁₆₈ 3.3.4 Comparison of MCMC Output to Expectation

₁₁₆₉ Whilst not important for the extraction of oscillation parameters, understanding how
₁₁₇₀ the data constrains the model parameters is important to the understanding of this
₁₁₇₁ analysis. A simple method of doing this is to perform a comparison in the fitting
₁₁₇₂ parameters (For instance, the reconstructed neutrino energy and lepton direction for
₁₁₇₃ T2K far detector beam samples) of the spectra generated by the MCMC chain to ‘data’.
₁₁₇₄ This ‘data’ could be true data or some variation of Monte Carlo prediction. This allows
₁₁₇₅ easy comparison of the MCMC probability distribution to the data. To perform this, N

1176 steps from the post burn-in MCMC chain are randomly selected (Where for all plots
1177 of this style in this thesis, $N = 3000$). From these, the Monte Carlo prediction at each
1178 step is generated by reweighting the model parameters to the values specified at that
1179 step. Due to the probability density being directly correlated with the density of steps
1180 in a certain region, parameter values close to the best fit value are most likely to be
1181 selected.

1182 In practice, for each bin of the fitting parameters has a probability distribution
1183 of event rates, with one entry per sampled MCMC step. This distribution is binned
1184 where the bin with the highest probability is selected as the mean and an error on
1185 the width of this probability distribution is calculated using the approach highlighted
1186 in subsection 3.3.2. Consequently, the best fit distribution in the fit parameter is not
1187 necessarily that which would be attained by reweighting the Monte Carlo prediction
1188 to the most probable parameter values.

1189 A similar study can be performed to illustrate the freedom of the model parameter
1190 space prior to the fit. This can be done by throwing parameter values from the prior
1191 uncertainty of each parameter. This becomes troublesome for parameters with no
1192 prior uncertainty as the range is technically infinite. Where applicable solutions to
1193 remove these have been addressed.

₁₁₉₄ **Chapter 4**

₁₁₉₅ **Oscillation Probability Calculation**

₁₁₉₆ **4.1 Overview**

₁₁₉₇ The analysis presented within this thesis focuses on the determination of oscillation
₁₁₉₈ parameters from atmospheric and beam neutrinos. Whilst subject to the same oscil-
₁₁₉₉ lation probability, the way in which the two sets of samples have sensitivity to the
₁₂₀₀ different oscillation parameters differs quite significantly.

₁₂₀₁ Atmospheric neutrinos have a varying baseline such that the distance each neutrino
₁₂₀₂ travels before interacting is dependent upon the zenith angle. Therefore the oscillation
₁₂₀₃ probability can be represented as a two-dimensional “oscillogram” as shown in Fig-
₁₂₀₄ ure 4.1. For this calculation, four layers of fixed density were used to model the Earth
₁₂₀₅ with values taken from an approximation of the PREM model. The oscillogram shows
₁₂₀₆ the different layers and how the oscillation probability reacts to them (The fourth layer,
₁₂₀₇ ‘inner core’, is very close to $\cos(\theta_Z) = -1.0$ and is not visible). **DB: I don’t know if I trust**
₁₂₀₈ **this.**

₁₂₀₉ Atmospheric neutrinos do have some sensitivity to δ_{CP} through a normalisa-
₁₂₁₀ tion term. Figure 4.2 illustrates the difference in oscillation probability between
₁₂₁₁ CP-conserving and CP-violating δ_{CP} values. The result is a complicated oscillation
₁₂₁₂ patter in the appearance probability for sub-GeV upgoing neutrinos. The detector does
₁₂₁₃ not have sufficient resolution to resolve these individual patterns so the sensitivity to
₁₂₁₄ δ_{CP} for atmospheric neutrinos comes via the overall normalisation of the sub-GeV

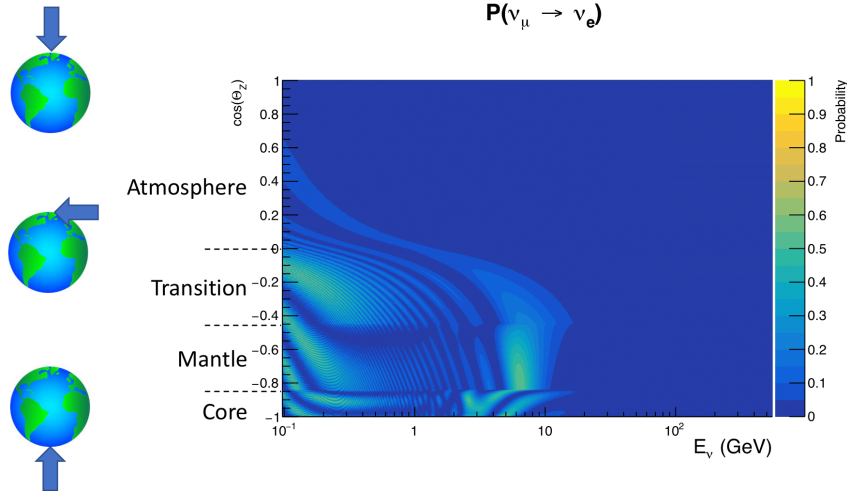


Figure 4.1: An “Oscillogram” that depicts the $P(\nu_\mu \rightarrow \nu_e)$ oscillation probability as a function of neutrino energy and cosine of the zenith angle. The zenith angle is defined such that $\cos(\Theta_Z) = 1.0$ represents neutrinos which travel from directly above the detector. The four layer constant density PREM model approximation is used and Asimov A oscillation parameters are assumed.

1215 upgoing events. The presence of matter means that the effect δ_{CP} has on the oscillation
 1216 probability is not equal between neutrinos and antineutrinos which would be expected
 1217 in vacuum. This is further extenuated by the fact that SK can not distinguish neutrinos
 1218 and antineutrinos well and that the cross section neutrino interaction is larger than
 1219 that for antineutrinos. Finally, sample selections (discussed in [DB: Link to selection](#)
 1220 [chapter](#)) targeting different neutrino interactions modes (charge current quasi-elastic
 1221 and single pion production) result in an imbalance in the percentage of neutrinos to
 1222 anti-neutrinos in these samples due to pion capture. Negatively charged pions from
 1223 antineutrino interactions are more likely to be captured by a nucleus compared to a
 1224 positively charged pion emitted from a neutrino interaction. This all culminates in
 1225 atmospheric neutrinos having a very complex sensitivity to δ_{CP} .

1226 Atmospheric neutrinos are subject to matter effects as they travel through the dense
 1227 matter in the Earth. The vacuum and matter oscillation probabilities for $P(\nu_e \rightarrow \nu_e)$
 1228 and $P(\bar{\nu}_e \rightarrow \bar{\nu}_e)$ are presented in Figure 4.3. The matter resonance occurs for neutrinos

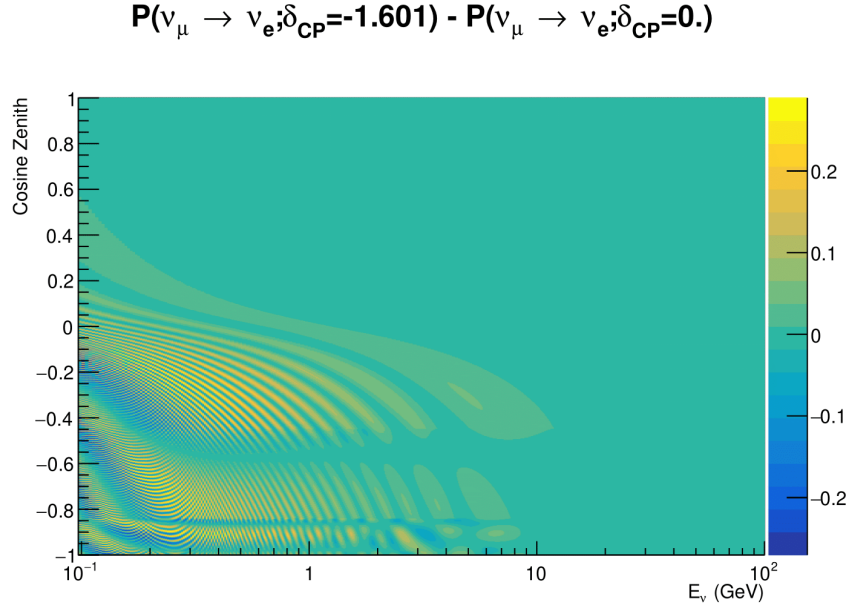


Figure 4.2

with $E_\nu = O(5)\text{GeV}$. The exact position and amplitude of the resonance depends on both $\sin^2(\theta_{23})$ meaning that the atmospheric neutrinos have sensitivity to the octant of θ_{23} . The matter resonance only occurs for neutrinos in normal mass hierarchy and antineutrinos for inverse mass ordering.

As the T2K beam flux is centered at the first oscillation maximum, the sensitivity to δ_{CP} is predominantly observed as a change in the event-rate of e-like samples in $\nu/\bar{\nu}$ modes. Figure 4.4 illustrates the $P(v_\mu \rightarrow v_e)$ oscillation probability for a range of δ_{CP} values. A circular modulation of the oscillation peak (in both magnitude and position) is observed when varying throughout the allowable values of δ_{CP} . The CP-conserving values of $\delta_{CP} = 0, \pi$ have a lower(higher) oscillation maximum than the CP-violating values of $\delta_{CP} = -\pi/2 (\delta_{CP} = \pi/2)$ leading to a $\sin \delta_{CP}$ type sensitivity. A sub-dominant shift in the energy of the oscillation peak is also present to aid separating the two CP-conserving value of δ_{CP} .

T2K's sensitivity to the atmospheric oscillation parameters is more of a shape-based variation of the muon-like samples, as illustrated in Figure 4.4. The value of

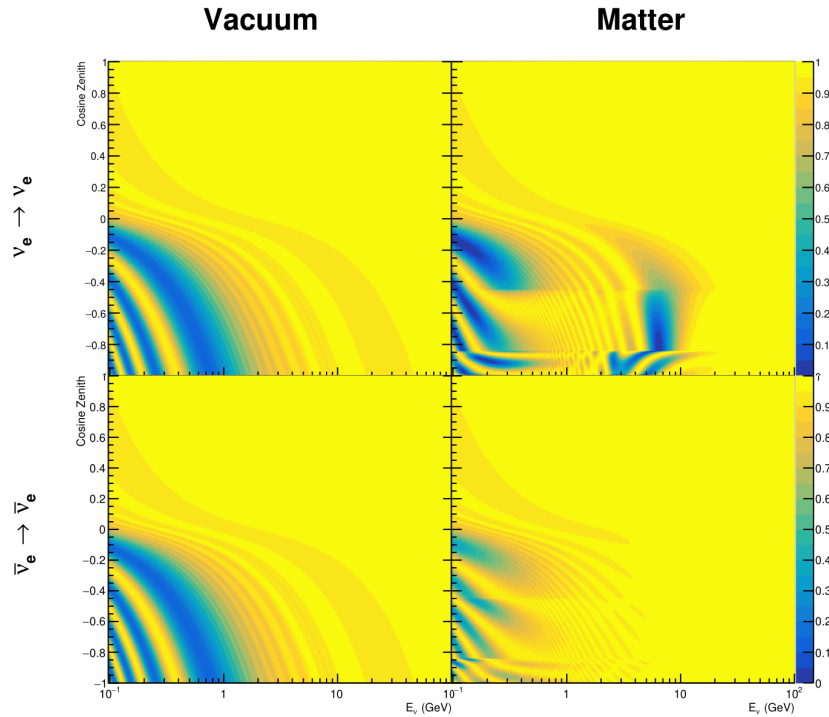


Figure 4.3

1244 Δm_{32}^2 laterally shifts the position of the oscillation dip (around $E_\nu \sim 0.6\text{GeV}$) in the
 1245 $P(\nu_\mu \rightarrow \nu_\mu)$ oscillation probability. The variation of $\sin^2(\theta_{23})$ is not as straight-forward
 1246 to interpret due to matter effects. The predominant effect is to vertically shift the
 1247 oscillation dip but matter effects also induce second order terms to laterally shift the
 1248 position of the dip.

1249 To allow comparisons between the joint analysis and the single experiment analyses,
 1250 two sets of oscillation parameters have been defined.

1251

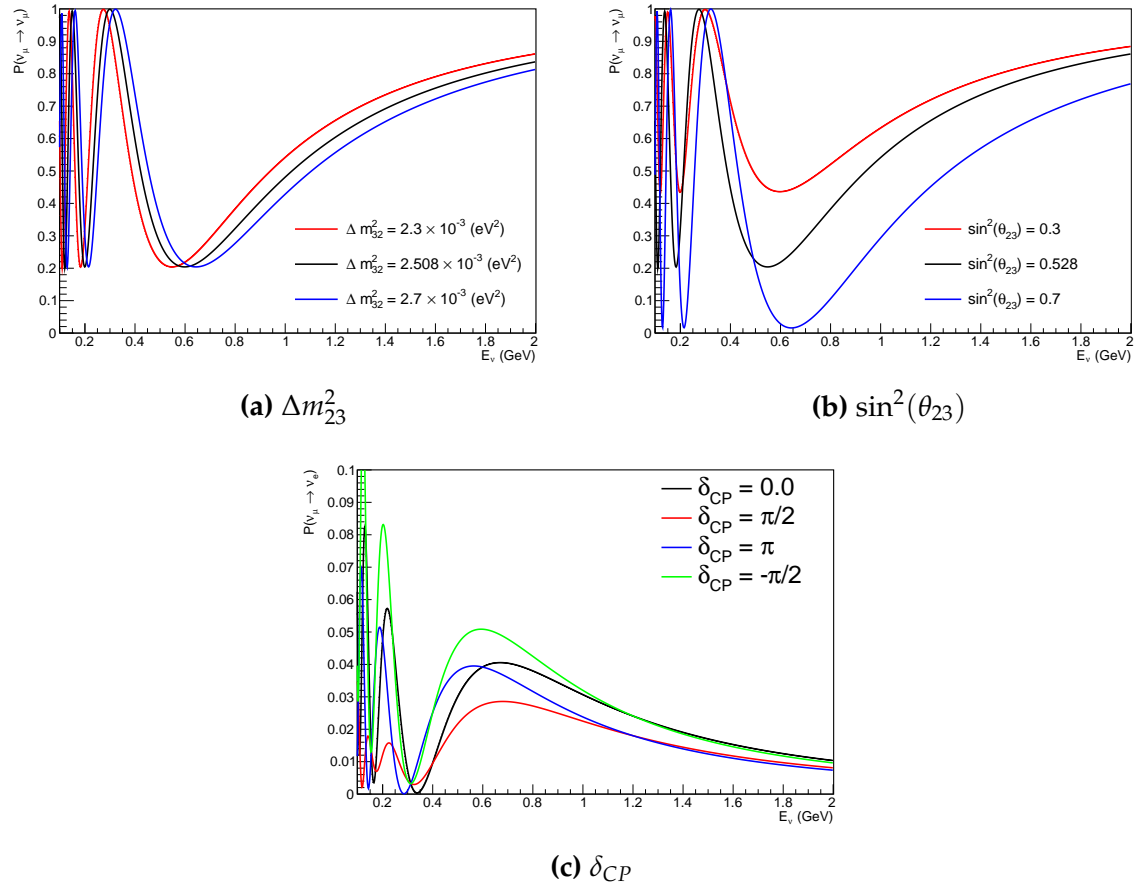


Figure 4.4

Parameter	Asimov A	Asimov B
Δm_{12}^2	$7.53 \times 10^{-5} \text{ eV}^2$	
Δm_{32}^2	$2.509 \times 10^{-3} \text{ eV}^2$	
$\sin^2(\theta_{12})$	0.304	
$\sin^2(\theta_{13})$	0.0219	
$\sin^2(\theta_{23})$	0.528	0.45
δ_{CP}	-1.601	0.0

Table 4.1

₁₂₅₂ **Bibliography**

- ₁₂₅₃ [1] J. Chadwick, Verhandl. Dtsc. Phys. Ges. **16**, 383 (1914).
- ₁₂₅₄ [2] C. D. Ellis and W. A. Wooster, Proc. R. Soc. Lond. A Math. Phys. Sci. **117**, 109
₁₂₅₅ (1927).
- ₁₂₅₆ [3] W. Pauli, Phys. Today **31N9**, 27 (1978).
- ₁₂₅₇ [4] E. Fermi, Z. Phys. **88**, 161 (1934).
- ₁₂₅₈ [5] F. Reines and C. L. Cowan, Phys. Rev. **92**, 830 (1953).
- ₁₂₅₉ [6] C. L. Cowan, F. Reines, F. B. Harrison, H. W. Kruse, and A. D. McGuire, Science
₁₂₆₀ **124**, 103 (1956), <http://science.sciencemag.org/content/124/3212/103.full.pdf>.
- ₁₂₆₁ [7] G. Danby *et al.*, Phys. Rev. Lett. **9**, 36 (1962).
- ₁₂₆₂ [8] K. Kodama *et al.*, Physics Letters B **504**, 218 (2001).
- ₁₂₆₃ [9] LSND, A. Aguilar-Arevalo *et al.*, Phys. Rev. **D64**, 112007 (2001), hep-ex/0104049.
- ₁₂₆₄ [10] MiniBooNE Collaboration, A. A. Aguilar-Arevalo *et al.*, Phys. Rev. Lett. **110**,
₁₂₆₅ 161801 (2013).
- ₁₂₆₆ [11] and P. A. R. Ade *et al.*, Astronomy and Astrophysics **594**, A13 (2016).
- ₁₂₆₇ [12] B. Pontecorvo, Sov. Phys. JETP **26**, 984 (1968), [Zh. Eksp. Teor. Fiz. 53, 1717 (1967)].
- ₁₂₆₈ [13] B. Pontecorvo, Sov. Phys. JETP **7**, 172 (1958), [Zh. Eksp. Teor. Fiz. 34, 247 (1957)].
- ₁₂₆₉ [14] M. Kobayashi and T. Maskawa, Progress of Theoretical Physics **49**, 652 (1973).
- ₁₂₇₀ [15] N. Cabibbo, Phys. Rev. Lett. **10**, 531 (1963).
- ₁₂₇₁ [16] A. Y. Smirnov, (2003).
- ₁₂₇₂ [17] S. Mikheyev and A. Smirnov, Soviet Journal of Nuclear Physics **42**, 913 (1985).
- ₁₂₇₃ [18] L. Wolfenstein, Phys. Rev. D **17**, 2369 (1978).
- ₁₂₇₄ [19] A. M. Dziewonski and D. L. Anderson, Phys. Earth Planet. Inter. **25**, 297 (1981).
- ₁₂₇₅ [20] R. Wendell, *Three Flavor Oscillation Analysis of Atmospheric Neutrinos in Super-Kamiokande*, PhD thesis, University of North Carolina, 2008.
₁₂₇₆

- 1277 [21] The Super-Kamiokande Collaboration, Y. Ashie *et al.*, Phys. Rev. Lett. **93**, 101801
1278 (2004).
- 1279 [22] SNO Collaboration, Q. R. Ahmad *et al.*, Phys. Rev. Lett. **89**, 011301 (2002).
- 1280 [23] 2015 Nobel prize in Physics as listed by Nobelprize.org, [https://www.](https://www.nobelprize.org/nobel_prizes/physics/laureates/2015/)
1281 [nobelprize.org/nobel_prizes/physics/laureates/2015/](https://www.nobelprize.org/nobel_prizes/physics/laureates/2015/), Accessed: 18-04-
1282 2018.
- 1283 [24] J. A. Formaggio and G. P. Zeller, Rev. Mod. Phys. **84**, 1307 (2012), 1305.7513.
- 1284 [25] A. Bellerive, Int. J. Mod. Phys. A **19**, 1167 (2004).
- 1285 [26] R. Davis, D. S. Harmer, and K. C. Hoffman, Phys. Rev. Lett. **20**, 1205 (1968).
- 1286 [27] N. Vinyoles *et al.*, Astrophys. J. **835**, 202 (2017).
- 1287 [28] V. Gribov and B. Pontecorvo, Phys. Lett. B **28**, 493 (1969).
- 1288 [29] K. S. Hirata *et al.*, Phys. Rev. Lett. **63**, 16 (1989).
- 1289 [30] W. Hampel *et al.*, Phys. Lett. B **447**, 127 (1999).
- 1290 [31] SAGE Collaboration, J. N. Abdurashitov *et al.*, Phys. Rev. C **60**, 055801 (1999).
- 1291 [32] Q. R. Ahmad *et al.*, Phys. Rev. Lett. **89** (2002).
- 1292 [33] Borexino Collaboration, Nature **562**, 505 (2018).
- 1293 [34] B. Aharmim *et al.*, Astrophys. J. **653**, 1545 (2006).
- 1294 [35] M. Agostini *et al.*, (2020).
- 1295 [36] S. Andringa *et al.*, Adv. High Energy Phys. **2016**, 1 (2016).
- 1296 [37] J. F. Beacom *et al.*, Chin. phys. C **41**, 023002 (2017).
- 1297 [38] F. An *et al.*, J. Phys. G Nucl. Part. Phys. **43**, 030401 (2016).
- 1298 [39] J. Aalbers *et al.*, (2020), 2006.03114.
- 1299 [40] T. K. Gaisser and M. Honda, (2002).
- 1300 [41] G. D. Barr, T. K. Gaisser, P. Lipari, S. Robbins, and T. Stanev, Physical Review D
1301 **70** (2004).
- 1302 [42] M. Honda, T. Kajita, K. Kasahara, S. Midorikawa, and T. Sanuki, Physical Review

- 1303 D **75** (2007).
- 1304 [43] M. Honda, T. Kajita, K. Kasahara, and S. Midorikawa, Phys. Rev. D **70**, 043008
1305 (2004).
- 1306 [44] A. Fasso, A. Ferrari, P. R. Sala, and J. Ranft, (2001).
- 1307 [45] Y. Ashie *et al.*, Physical Review D **71** (2005).
- 1308 [46] F. Reines *et al.*, Phys. Rev. Lett. **15**, 429 (1965).
- 1309 [47] D. Casper *et al.*, Phys. Rev. Lett. **66**, 2561 (1991).
- 1310 [48] K. S. Hirata *et al.*, Phys. Lett. B **280**, 146 (1992).
- 1311 [49] Z. Li *et al.*, Physical Review D **98** (2018).
- 1312 [50] Kamiokande Collaboration *et al.*, (2017).
- 1313 [51] T2K Collaboration, Nature **580**, 339 (2020).
- 1314 [52] M. A. Acero *et al.*, Phys. Rev. Lett. **123**, 151803 (2019).
- 1315 [53] M. G. Aartsen *et al.*, Phys. Rev. Lett. **120** (2018).
- 1316 [54] P. Adamson *et al.*, Phys. Rev. Lett. **112** (2014).
- 1317 [55] M. S. Athar *et al.*, Progress in Particle and Nuclear Physics **124**, 103947 (2022).
- 1318 [56] G. Danby *et al.*, Phys. Rev. Lett. **9**, 36 (1962).
- 1319 [57] K. Abe *et al.*, Physical Review D **87** (2013).
- 1320 [58] MINOS Collaboration, D. G. Michael *et al.*, Phys. Rev. Lett. **97**, 191801 (2006).
- 1321 [59] G. Danby *et al.*, Phys. Rev. Lett. **9**, 36 (1962).
- 1322 [60] NOvA Collaboration, M. A. Acero *et al.*, Phys. Rev. Lett. **123**, 151803 (2019).
- 1323 [61] B. Abi, R. Acciarri, M. A. Acero, and G. e. a. Adamov, Eur. Phys. J. C Part. Fields
1324 **80** (2020).
- 1325 [62] Hyper-Kamiokande Proto-Collaboration *et al.*, Prog. Theor. Exp. Phys. **2015**,
1326 53C02 (2015).
- 1327 [63] C. Blanco, D. Hooper, and P. Machado, Physical Review D **101** (2020).
- 1328 [64] MicroBooNE Collaboration *et al.*, Search for an Excess of Electron Neutrino

- 1329 Interactions in MicroBooNE Using Multiple Final State Topologies, 2021.
- 1330 [65] KARMEN Collaboration, B. Armbruster *et al.*, Phys. Rev. D **65**, 112001 (2002).
- 1331 [66] S.-B. Kim, T. Lasserre, and Y. Wang, Adv. High Energy Phys. **2013**, 1 (2013).
- 1332 [67] M. Sajjad Athar *et al.*, Prog. Part. Nucl. Phys. **124**, 103947 (2022), 2111.07586.
- 1333 [68] K. Abe *et al.*, Nucl. Instrum. Methods Phys. Res. A **1027**, 166248 (2022).
- 1334 [69] F. P. An *et al.*, Phys. Rev. Lett. **108**, 171803 (2012).
- 1335 [70] RENO Collaboration, J. K. Ahn *et al.*, Phys. Rev. Lett. **108**, 191802 (2012).
- 1336 [71] Double Chooz Collaboration, Y. Abe *et al.*, Phys. Rev. Lett. **108**, 131801 (2012).
- 1337 [72] J. Collaboration *et al.*, TAO Conceptual Design Report: A Precision Measurement
1338 of the Reactor Antineutrino Spectrum with Sub-percent Energy Resolution, 2020,
1339 2005.08745.
- 1340 [73] for the RENO Collaboration, New results from RENO and the 5 MeV excess,
1341 AIP Publishing LLC, 2015.
- 1342 [74] Y. Abe *et al.*, Journal of High Energy Physics **2014** (2014).
- 1343 [75] Daya Bay Collaboration, D. Adey *et al.*, Phys. Rev. Lett. **123**, 111801 (2019).
- 1344 [76] M. P. Decowski, Nucl. Phys. B. **908**, 52 (2016).
- 1345 [77] The KamLAND Collaboration, A. Gando *et al.*, Phys. Rev. D **83**, 052002 (2011).
- 1346 [78] Y. Fukuda *et al.*, Phys. Rev. Lett. **81**, 1562 (1998).
- 1347 [79] K. Abe *et al.*, Nuclear Instruments and Methods in Physics Research Section
1348 A: Accelerators, Spectrometers, Detectors and Associated Equipment **737**, 253
1349 (2014).
- 1350 [80] S. Fukuda *et al.*, Nucl. Instrum. Methods Phys. Res. A **501**, 418 (2003).
- 1351 [81] Y. Itow *et al.*, (2001).
- 1352 [82] M. Jiang *et al.*, Prog. Theor. Exp. Phys. **2019** (2019).
- 1353 [83] S. Fukuda *et al.*, Nuclear Instruments and Methods in Physics Research Section
1354 A: Accelerators, Spectrometers, Detectors and Associated Equipment **501**, 418
1355 (2003), <http://www.sciencedirect.com/science/article/pii/S016890020300425X>.

- 1356 [84] Y. Nakano *et al.*, Nucl. Instrum. Methods Phys. Res. A **977**, 164297 (2020).
- 1357 [85] Hamamatsu, Hamamatsu Photonics Photomultiplier Tubes Handbook.
- 1358 [86] K. Abe *et al.*, Nucl. Instrum. Methods Phys. Res. A **1027**, 166248 (2022).
- 1359 [87] J. F. Beacom and M. R. Vagins, Phys. Rev. Lett. **93**, 171101 (2004).
- 1360 [88] L. Marti *et al.*, Nucl. Instrum. Methods Phys. Res. A **959**, 163549 (2020).
- 1361 [89] L. Marti *et al.*, (2019).
- 1362 [90] G. Carminati, Phys. Procedia **61**, 666 (2015).
- 1363 [91] T. Tanimori *et al.*, IEEE Transactions on Nuclear Science **36**, 497 (1989).
- 1364 [92] Super-Kamiokande Collaboration, J. Hosaka *et al.*, Phys. Rev. D **73**, 112001
1365 (2006).
- 1366 [93] H. Nishino *et al.*, Nucl. Instrum. Methods Phys. Res. A **610**, 710 (2009).
- 1367 [94] S. Yamada *et al.*, IEEE Transactions on Nuclear Science **57**, 428 (2010).
- 1368 [95] S. Yamada, Y. Hayato, Y. Obayashi, and M. Shiozawa, New online system
1369 without hardware trigger for the Super-Kamiokande experiment, in *2007 IEEE
1370 Nuclear Science Symposium Conference Record*, IEEE, 2007.
- 1371 [96] P. A. Čerenkov, Phys. Rev. **52**, 378 (1937).
- 1372 [97] I. Frank and I. Tamm, Coherent visible radiation of fast electrons passing
1373 through matter, in *Selected Papers*, pp. 29–35, Springer Berlin Heidelberg, Berlin,
1374 Heidelberg, 1991.
- 1375 [98] The T2K Collaboration, KEK Proposal (2001),
1376 <http://neutrino.kek.jp/jhfnu/loi/loi.v2.030528.pdf>.
- 1377 [99] Y. Itow *et al.*, (2001), hep-ex/0106019.
- 1378 [100] The K2K Collaboration and S. H. Ahn, (2001), hep-ex/0103001.
- 1379 [101] The T2K Collaboration, KEK Proposal (2006), http://j-parc.jp/researcher/Hadron/en/pac_0606/pdf/p11-Nishikawa.pdf.
- 1380 [102] T2K Collaboration, K. Abe *et al.*, Phys. Rev. Lett. **112**, 061802 (2014),
1382 <https://link.aps.org/doi/10.1103/PhysRevLett.112.061802>.

- 1383 [103] NINJA Collaboration, T. Fukuda *et al.*, Proposal for precise measurement of
1384 neutrino-water cross-section in NINJA physics run, Proposal for J-PARC and
1385 KEK, 2017.
- 1386 [104] T. Ovsianikova *et al.*, Physics of Particles and Nuclei **48**, 1014 (2017),
1387 <https://doi.org/10.1134/S1063779617060478>.
- 1388 [105] M. Antonova *et al.*, Journal of Instrumentation **12**, C07028 (2017),
1389 <http://stacks.iop.org/1748-0221/12/i=07/a=C07028>.
- 1390 [106] The T2K Collaboration, K. Abe *et al.*, Phys. Rev. D **102**, 012007 (2020).
- 1391 [107] K. Abe *et al.*, Progress of Theoretical and Experimental Physics **2021** (2021).
- 1392 [108] The T2K Collaboration, K. Abe *et al.*, Nuclear Instruments
1393 and Methods in Physics Research Section A: Accelerators, Spec-
1394 trometers, Detectors and Associated Equipment **659**, 106 (2011),
1395 <http://www.sciencedirect.com/science/article/pii/S0168900211011910>.
- 1396 [109] K. Matsuoka *et al.*, Nuclear Instruments and Methods in Physics Research Section
1397 A: Accelerators, Spectrometers, Detectors and Associated Equipment **624**, 591
1398 (2010), <http://www.sciencedirect.com/science/article/pii/S016890021002098X>.
- 1399 [110] K. Abe *et al.*, Phys. Rev. D. **103** (2021).
- 1400 [111] T. Vladislavljevic, *Predicting the T2K neutrino flux and measuring oscillation parame-*
1401 *ters* Springer theses, 1 ed. (Springer Nature, Cham, Switzerland, 2020).
- 1402 [112] D. Beavis, A. Carroll, and I. Chiang, (1995).
- 1403 [113] P.-A. Amaudruz *et al.*, Nuclear Instruments and Methods in Physics Research
1404 Section A: Accelerators, Spectrometers, Detectors and Associated Equipment
1405 **696**, 1 (2012).
- 1406 [114] N. Abgrall *et al.*, Nuclear Instruments and Methods in Physics Research Section
1407 A: Accelerators, Spectrometers, Detectors and Associated Equipment **637**, 25
1408 (2011).
- 1409 [115] S. Assylbekov *et al.*, Nuclear Instruments and Methods in Physics Research
1410 Section A: Accelerators, Spectrometers, Detectors and Associated Equipment
1411 **686**, 48 (2012).
- 1412 [116] D. Allan *et al.*, Journal of Instrumentation **8**, P10019 (2013).

- ¹⁴¹³ [117] F. Vannucci, Advances in High Energy Physics **2014**, 1 (2014).
- ¹⁴¹⁴ [118] UA1 magnet sets off for a second new life, 2022.
- ¹⁴¹⁵ [119] S. Aoki *et al.*, Nuclear Instruments and Methods in Physics Research Section
¹⁴¹⁶ A: Accelerators, Spectrometers, Detectors and Associated Equipment **698**, 135
¹⁴¹⁷ (2013).
- ¹⁴¹⁸ [120] M. Yokoyama *et al.*, Nuclear Instruments and Methods in Physics Research
¹⁴¹⁹ Section A: Accelerators, Spectrometers, Detectors and Associated Equipment
¹⁴²⁰ **622**, 567 (2010).
- ¹⁴²¹ [121] K. Suzuki *et al.*, Progress of Theoretical and Experimental Physics **2015**, 53C01
¹⁴²² (2015).
- ¹⁴²³ [122] S. Brooks, A. Gelman, G. L. Jones, and X.-L. Meng, *Handbook of Markov Chain
Monte Carlo* (CRC Press, 2011).
- ¹⁴²⁵ [123] W. R. Gilks, S. Richardson, and D. J. Spiegelhalter, *Markov Chain Monte Carlo in
Practice* (Chapman & Hall/CRC Interdisciplinary Statistics, 1995).
- ¹⁴²⁷ [124] C. Wret, *Minimising systematic uncertainties in the T2K experiment using near-
detector and external data*, PhD thesis, Imperial College London, 2018.
- ¹⁴²⁹ [125] K. E. Duffy, *Measurement of the Neutrino Oscillation Parameters $\sin^2 \theta_{23}$, Δm_{32}^2 ,
 $\sin^2 \theta_{13}$, and δ_{CP} in Neutrino and Antineutrino Oscillation at T2K*, PhD thesis, Oriel
¹⁴³⁰ College, University of Oxford, 2016.
- ¹⁴³¹
- ¹⁴³² [126] T. Bayes, Rev. Phil. Trans. Roy. Soc. Lond. **53**, 370 (1764).
- ¹⁴³³ [127] N. Metropolis, A. W. Rosenbluth, M. N. Rosenbluth, A. H. Teller, and E. Teller,
¹⁴³⁴ Journal of Chemical Physics **21** (1970).
- ¹⁴³⁵ [128] W. K. Hastings, Biometrika **57** (1970).
- ¹⁴³⁶ [129] J. Dunkley, M. Bucher, P. G. Ferreira, K. Moodley, and C. Skordis, Mon. Not. R.
¹⁴³⁷ Astron. Soc. **356**, 925 (2005).
- ¹⁴³⁸ [130] Particle Data Group *et al.*, Prog. Theor. Exp. Phys. **2020** (2020).
- ¹⁴³⁹ [131] H. Jeffreys, *The Theory of Probability* Oxford Classic Texts in the Physical Sciences
¹⁴⁴⁰ (, 1939).
- ¹⁴⁴¹ [132] R. E. Kass and A. E. Raftery, J. Am. Stat. Assoc. **90**, 773 (1995).

¹⁴⁴² List of Figures

¹⁴⁴³ 1.1	The cross-section of neutrinos from various natural and man-made sources as a function of neutrino energy. Taken from [24]	10
¹⁴⁴⁴		
¹⁴⁴⁵ 1.2	The solar neutrino flux as a function of neutrino energy for various fusion reactions and decay chains as predicted by the Standard Solar Model. Taken from [25].	11
¹⁴⁴⁶		
¹⁴⁴⁷		
¹⁴⁴⁸ 1.3	Left panel: The atmospheric neutrino flux for different neutrino flavours as a function of neutrino energy as predicted by the 2007 Honda model (“This work”) [42], the 2004 Honda model (“HKKM04”) [43], the Bartol model [41] and the FLUKA model [44]. Right panel: The ratio of the muon to electron neutrino flux as predicted by all the quoted models. Both figures taken from [42].	13
¹⁴⁴⁹		
¹⁴⁵⁰		
¹⁴⁵¹		
¹⁴⁵²		
¹⁴⁵³		
¹⁴⁵⁴ 1.4	A diagram illustrating the definition of zenith angle as used in the Super Kamiokande experiment [45].	14
¹⁴⁵⁵		
¹⁴⁵⁶ 1.5	Predictions of the summed neutrino and antineutrino flux for electron and muon neutrinos from the Bartol [41], Honda [42] and FLUKA [44] models as a function of zenith angle with respect to the detector. Left panel: $0.3 < E_\nu < 0.5$. Middle panel: $0.9 < E_\nu < 1.5$. Right panel: $3.0 < E_\nu < 5.0$. Figures taken from [45].	15
¹⁴⁵⁷		
¹⁴⁵⁸		
¹⁴⁵⁹		
¹⁴⁶⁰		
¹⁴⁶¹ 1.6	Constraints on the atmospheric oscillation parameters, $\sin^2(\theta_{23})$ and Δm_{23}^2 , from atmospheric and long baseline experiments: SK [50], T2K [51], NO ν A [52], IceCube [53] and MINOS [54]. Figure taken from [55].	16
¹⁴⁶²		
¹⁴⁶³		
¹⁴⁶⁴ 1.7	Reactor electron antineutrino fluxes for ^{235}U (Black), ^{238}U (Green), ^{239}Pu (Purple), and ^{241}Pu (Orange) isotopes. The inverse β -decay cross-section (Blue) and corresponding measurable neutrino spectrum (Red) are also given. Top panel: Schematic of Inverse β -decay interaction including the eventual capture of the emitted neutron. This capture emits a γ -ray which provides a second signal of the event. Taken from [67].	19
¹⁴⁶⁵		
¹⁴⁶⁶		
¹⁴⁶⁷		
¹⁴⁶⁸		
¹⁴⁶⁹		
¹⁴⁷⁰ 2.1	A schematic diagram of the Super-Kamiokande Detector. Taken from [81].	23

1471	2.2	The location of “standard PMTs” (red) inside the SK detector. Taken from [79].	27
1472			
1473	2.3	Schematic view of the data flow through the data acquisition and online system. Taken from [94].	30
1474			
1475	2.4	The cross-section view of the Tokai to Kamioka experiment illustrating the beam generation facility at J-PARC, the near detector situated at a baseline of 280m and the Super Kamiokande far detector situated 295km from the beam target.	33
1476			
1477			
1478			
1479	2.5	The near detector suite for the T2K experiment showing the ND280 and INGRID detectors. The distance between the detectors and the beam target is 280m.	34
1480			
1481			
1482	2.6	Top panel: Bird’s eye view of the most relevant part of primary and secondary beamline used within the T2K experiment. The primary beamline is the main-ring proton synchrotron, kicker magnet, and graphite target. The secondary beamline consists of the three focusing horns, decay volume, and beam dump. Figure taken from [108]. Bottom panel: The side-view of the secondary beamline including the focusing horns, beam dump and neutrino detectors. Figure taken from [109].	36
1483			
1484			
1485			
1486			
1487			
1488			
1489	2.7	The Monte Carlo prediction of the energy spectrum for each flavour of neutrino (ν_e , $\bar{\nu}_e$, ν_μ and $\bar{\nu}_\mu$) in the neutrino dominated beam FHC mode (Left) and antineutrino dominated beam RHC mode (Right) expected at SK. Taken from [110].	37
1490			
1491			
1492			
1493	2.8	Top panel: T2K muon neutrino disappearance probability as a function of neutrino energy. Middle panel: T2K electron neutrino appearance probability as a function of neutrino energy. Bottom panel: The neutrino flux distribution for three different off-axis angles (Arbitrary units) as a function of neutrino energy.	39
1494			
1495			
1496			
1497			
1498	2.9	The components of the ND280 detector. The neutrino beam travels from left to right. Taken from [108].	40
1499			
1500	2.10	Comparison of data to Monte Carlo prediction of integrated deposited energy as a function of track length for particles that stopped in FGD1. Taken from [113].	42
1501			
1502			

1503	2.11 Schematic design of a Time Projection Chamber detector. Taken from [114].	43
1504	2.12 The distribution of energy loss as a function of reconstructed momentum for charged particles passing through the TPC, comparing data to Monte Carlo prediction. Taken from [114].	43
1505		
1506		
1507	2.13 A schematic of the P0D side-view. Taken from [115].	45
1508	2.14 Left panel: The Interactive Neutrino GRID on-axis Detector. 14 modules are arranged in a cross-shape configuration, with the center modules being directly aligned with the on-axis beam. Right panel: The layout of a single module of the INGRID detector. Both figures are recreated from [108].	47
1509		
1510		
1511		
1512		
1513	3.1 Example of using Monte Carlo techniques to find the area under the blue line. The gradient and intercept of the line are 0.4 and 1.0 respectively. The area found to be under the curve using one thousand samples is 29.9 units.	52
1514		
1515		
1516		
1517	3.2 The area under a line of gradient 0.4 and intercept 1.0 for the range $0 \leq x \leq 10$ as calculated using Monte Carlo techniques as a function of the number of samples used in each repetition. The analytical solution to the area is 30 units as given by the red line.	53
1518		
1519		
1520		
1521	3.3 Three MCMC chains, each with a stationary distribution equal to a Gaussian centered at 0 and width 1 (As indicated by the black dotted lines). All of the chains use a Gaussian proposal function but have different widths (or ‘step size σ ’). The top panel has $\sigma = 0.1$, middle panel has $\sigma = 0.5$ and the bottom panel has $\sigma = 5.0$.	58
1522		
1523		
1524		
1525		
1526	3.4 The log-likelihood from the fit detailed in DB: Link to AsimovA Sensitivity Section as a function of the number of steps accumulated in each fit. Many independent MCMC chains were run in parallel and overlaid on this plot. The red line indicates the 1×10^5 step burn-in period after which the log-likelihood becomes stable.	59
1527		
1528		
1529		
1530		

1531	3.5	Left: The two dimensional probability distribution for two correlated parameters x and y . The red distribution shows the two dimensional probability distribution when $0 \leq x \leq 5$. Right: The marginalised probability distribution for the y parameter found when requiring the x to be bound between $-5 \leq x \leq 5$ and $0 \leq x \leq 5$ for the black and red distribution, respectively.	62
1537	4.1	An “Oscillogram” that depicts the $P(\nu_\mu \rightarrow \nu_e)$ oscillation probability as a function of neutrino energy and cosine of the zenith angle. The zenith angle is defined such that $\cos(\Theta_Z) = 1.0$ represents neutrinos which travel from directly above the detector. The four layer constant density PREM model approximation is used and Asimov A oscillation parameters are assumed.	67
1543	4.2	68
1544	4.3	69
1545	4.4	70

List of Tables

1547	1.1	Description of the four layers of the Earth invoked within the PREM model [19].	9
1548			
1549	2.1	The various SK periods and respective live-time. The SK-VI live-time is calculated until 1 st April 2022. SK-VII started during the writing of this thesis.	22
1550			
1551	2.2	The trigger thresholds and extended time windows saved around an event which were utilised throughout the SK-IV period. The exact thresholds can change and the values listed here represent the thresholds at the start and end of the SK-IV period.	31
1552			
1553	2.3	The threshold momentum and energy for a particle to generate Cherenkov light in ultrapure water, as calculated in Equation 2.2 in ultrapure water which has refractive index $n = 1.33$	32
1554			
1555	3.1	Jeffreys scale for strength of preference for two models A and B as a function of the calculated Bayes factor ($B_{AB} = B(A/B)$) between the two models [131]. The original scale is given in terms of $\log_{10}(B(A/B))$ but converted to linear scale for easy comparison throughout this thesis.	64
1556			
1557			
1558			
1559	4.1	70
1560			
1561			
1562			
1563			